1 **W-band S/Z Relationships for Rimed Snow Particles: Observational Evidence from**

2 **Combined Airborne and Ground-based Observations**

3

4 Shelby Fuller [1], Sam Marlow [1], Samuel Haimov [1], Matthew Burkhart [1], Kevin Shaffer [1], Austin

5 Morgan [1], and Jefferson R. Snider [1,2]

6

7 [1] Department of Atmospheric Science, University of Wyoming, Laramie, WY, USA
8
9
10
11 [2] Corresponding Author, jsnider@uwyo.edu
12

Abstract

13

14   Values of undercatch-corrected liquid-equivalent snowfall rate (S) at a ground site and

15   microwave reflectivity (Z) retrieved using an airborne W-band radar were acquired during

16   overflights. The temperature at the ground site was between -6 and -15 $^{\circ}$C. At flight level, within

17   clouds containing ice and supercooled liquid water, the temperature was approximately 7 $^{\circ}$C

18   colder. Additionally, airborne measurements of snow particle imagery were acquired. The

19   images demonstrate that most of the snow particles were rimed, at least a flight level. A

20   relatively small set of S/Z pairs (4) are available from the overflights. Important distinctions

21   between these measurements and those of Pokharel and Vali (2011), who reported S/Z pairs and

22   an S/Z relationship for rimed snow particles, are 1) the fewer number of S/Z pairs, 2) the method

23   used to acquire S, and 3) the altitude, relative to ground, of the W-band Z retrievals. This

24   analysis corroborates that the S/Z relationship reported in Pokharel and Vali (2011) yields an S -

25   in scenarios with snowfall produced by riming - substantially larger than that derived using an

26   S/Z relationship developed for unrimed snow particles.

27

28

29   **1 - Introduction**

30   Improvement of methods used to measure snowfall and rainfall are an ongoing focus of

31   meteorological research. The various methods are ground-based instruments that evaluate the

32   mass of precipitation that falls into or onto a collector (precipitation gauges) (Brock and

33   Richardson 2001), ground-based radars (Wilson and Brandes 1979), and airborne and space-

34   borne radars (Matrosov 2007; Kulie and Bennartz 2009; Geerts et al. 2010; Skofronick-Jackson

35   et al. 2017). An objective of these approaches, whether used to make observations independent

36   of other methods (e.g., Kulie and Bennartz 2009), or as a component of multiple observations

37   (e.g., Cocks et al. 2016), is estimation of precipitation rate and accumulated precipitation

38   amount.

39   Many studies have investigated using radar for evaluating rainfall (for a review see

40   Wilson and Brandes 1979). There are two approaches. The first is research, both observational

41   and computational, that probes the relationship between rainfall rate (R) and radar-measured

42   values of range-corrected backscattered microwave power. The latter is commonly reported as an

43   equivalent radar reflectivity factor (Z_e). The second is operational in the sense that precipitation

44   gauges are used to calibrate measurements acquired using weather surveillance radars.

45   Complications associated with converting Z_e to R, or converting a radar reflectivity factor[1] (Z) to

46   R, can be grouped in four categories: 1) Inaccuracy in quantification of Z, 2) variation of the

47   R/Z relationship stemming from precipitation processes (e.g., coalescence and break up), 3)

48   difference between the volume of a radar range gate versus the much smaller volume of

---

[1] Radars are calibrated to report Z_e (Smith 1984). Herein, radar reflectivities are reported as $Z = Z_e$ and as $dBZ = 10\log_{10}(Z_e)$.

49 atmosphere sampled as precipitation falls to a gauge, and 4) vertical displacement between a

50 radar range gate and a calibrating gauge, especially at far ranges.

51   For situations with snowfall, methods employing either gauge or radar are associated

52 with complications beyond that incurred in rainfall (Matrosov 2007; Martinaitis et al. 2015;

53 Cocks et al. 2016). Problems associated with gauge measurements are wind-induced snow

54 particle undercatch, gauge capping, delayed registration, and blowing snow aliasing as snowfall.

55 Moreover, in a situation with snow particles more abundant within a radar range gate, compared

56 to rain drops, and where a measurement of Z is used to infer R via an R/Z relationship, the

57 resultant precipitation rate will likely be inaccurate. This is because hydrometeor shape, density,

58 and dielectric properties are all variable for snow particles while relatively invariant for rain

59 drops. Additionally, a snow particle's terminal fall speed varies with size (as is the case for

60 drops) and with particle shape and particle density. Going forward, we refer to the latter two

61 properties as shape and density.

62   The goals of this paper are as follows: 1) to describe measurements of undercatch-

63 corrected liquid-equivalent snowfall rate (S, mm h^{-1}) and how these were paired with W-band

64 measurements of reflectivity (Z, mm^6 m^{-3}) ; 2) to contrast the S/Z pairs against S/Z relationships

65 commonly applied in radar retrievals of S; and 3) to investigate why the S/Z pairs deviate from

66 predictions of some S/Z relationships.

67   In calculations of paired values of S and Z, density is an important parameter. Density is

68 commonly estimated using empirical data (e.g., Pokharel and Vali 2011, [PV11]). For graupel, a

69 snow particle that grows via collection of supercooled cloud droplets in a process commonly

70 referred to as riming, paired observations of particle mass and particle size have been used to

71 estimate density. There is considerable uncertainty in this approach. Based on data collected at

72 two northwestern US surface sites (Zikmunda and Vali 1972; Locatelli and Hobbs 1974), density

73 values differ by at least a factor of two at particle sizes smaller than 2000 μm (PV11; their Fig.

74 4). Given that the density of rime ice varies with droplet impact speed, droplet size, and

75 temperature (Macklin 1962), it is not surprising that the density-size relationships analyzed by

76 PV11 are so varied.

77   Table 1 and the following paragraphs overview W-band S/Z relationships applied in

78 instances with snow particles grown by vapor deposition (crystal), by collection of crystals

79 (aggregate snowflake), and by riming (rimed crystal and graupel). Henceforth, the latter two

80 snow particle types are collectively referred to as rimed snow particles.

81   In a computational study, Hiley et al. (2011) considered a variety of snow particle types

82 (column, plate, bullet rosette, sector plate, dendrite, and aggregate snowflake), employed a

83 parameterized ice particle size distribution (PSD) function (Field et al. 2005), accounted for a

84 range of temperature (-5 to -15 ^{o}C) via the Field et al. parameterization, and developed a range of

85 S/Z relationships for snow particles. Except for the aggregate snowflakes (henceforth,

86 aggregates), the modeled particle types were vapor-grown crystals. Hiley et al.'s upper- and

87 lower-limit relationships are $S = 0.21 \cdot Z^{0.77}$ and $S = 0.024 \cdot Z^{0.91}$, respectively. Matrosov (2007)

88 developed an S/Z relationship for aggregates. In that work, parameterized PSDs from Braham

89 (1990) were employed, and a range of particle aspect ratios were factored into the calculations.

90 For aggregates, the S/Z relationship is $S = 0.056 \cdot Z^{1.2}$ (Matrosov 2007). It should be noted that

91 Hiley et al. (2011) and Matrosov (2007) employed similar, but not identical, computational

92 methods. Computational research was also conducted by Kulie and Bennartz (2009) who

93 adopted the wavelength-dependent density derived by Surussavadee and Staelin (2007) (200 kg

94 m^{-3} at λ = 3.2 mm), modeled the snow particles as spheres, and applied PSDs based on Field et

95   al. The resultant S/Z is $S = 0.52 \cdot Z^{0.83}$ (Surussavadee and Staelin 2007; Kulie and Bennartz 2009;

96   henceforth, SSKB). Variance in the calculations discussed in this paragraph originate from

97   changes in density, shape, fall speed, PSD, and particle size as these changes are propagated

98   through the cloud-microphysical and microwave-scattering calculations.

99   In a hybrid approach (computational and an analysis of measurements), PV11 concluded

100   that most of the snow particles they imaged were rimed snow particles. Values of S were

101   calculated using a density-size function (ρ_1, discussed below), a fall speed-size function,

102   measured PSDs and measured particle images, and a determination of particle volumes. It was

103   assumed that a prolate spheroid approximated particle shape and that shape was the basis for

104   determining a particle's sphere-equivalent volume and the particle's sphere-equivalent size. The

105   sphere-equivalent size was applied in the two functions. Values of Z were calculated using a

106   measured PSD, sphere-equivalent sizes, the ρ_1 function, and Mie Theory. PV11 presented

107   calculations of Z, obtained using two density-size relationships (their Eqs. 1 and 2) and compared

108   their calculated reflectivities to measurements of Z from a W-band radar. That led to their

109   conclusion that "...the lower density assumption…yielded closer correspondence to observed

110   reflectivities." Their recommendation for S as a function of measured Z - hereafter the $S(\rho_1)$/Z

111   best-fit line - is $S = 0.39 \cdot Z^{0.58}$. Values of Z that were paired with the calculated values of S (i.e.,

112   the S/Z pairs from PV11 that we present in Sect. 4), and that were used to determine the $S(\rho_1)$/Z

113   best-fit line, came from the WCR. In addition to variance in their values of S, coming from a

114   dependence on density, PV11 state that a value of S derived via their best-fit line is uncertain by

115   a factor-of-ten. That uncertainty is evident in the variance of S/Z data pairs about the $S(\rho_1)$/Z line

116   in Fig. 11 of PV11. Those investigators, and Geerts et al. (2010), attributed the variance to use of

117 two-dimensional snow particle images in calculations of S and to actual variations of density,

118 shape, and particle size not accounted for in the calculations.

119   Another set of hybrid-type S/Z relationships was developed by Falconi et al. (2018; their

120 Table 2). These are based on measurements from a video disdrometer, weighing precipitation

121 gauge, microwave radiometer, and a vertically-pointing W-band radar. All these systems were

122 operated at the ground. The data set was stratified into intervals of lightly-rimed, moderately-

123 rimed, and heavily-rimed snow. A proxy for snow particle riming - radiometer measurements of

124 liquid water path – was the basis for the stratifications (von Lerber et al. 2017). The S/Z

125 relationships are $S = 0.10 \cdot Z^{1.0}$ (lightly-rimed), $S = 0.079 \cdot Z^{1.3}$ (moderately-rimed), and $S =$

126 $0.060 \cdot Z^{1.4}$ (heavily-rimed).

127   Our focus is on surface measurements of S and on pairing of those measurements with

128 airborne measurements of Z. We also analyze airborne measurements of snow particle imagery.

129 The latter demonstrate that the particles observed at flight level were rimed. The imagery is the

130 basis for our assertion that our data set is relevant to ongoing investigations of using Z to

131 evaluate S in situations where precipitation is produced by riming.

132   Section 2 describes the setting of our study, the instruments we deployed, and recordings

133 we obtained using two data acquisition systems. One of the data systems was operated at a

134 ground site and the other on an aircraft. Section 3 is an analysis of the recordings; this section

135 also considers recordings from two additional, but ancillary, ground sites. Our findings are

136 discussed in Sect. 4 and summarized in Sect. 5. An Appendix (Sect. 6) explains how we

137 averaged recordings of near-surface W-band reflectivities and surface-based recordings of

138 snowfall.

139 Table 1 – W-band S/Z relationships from the literature, snow particle type, and values of minimum relative S difference

Reference	Abbreviation used for reference	S/Z relationship	Snow Particle Type	Minimum relative S deference on December 15 2016 [a]	Minimum relative S difference on January 3 2017 [a]
Hiley et al. (2011)	-	$S=0.21 \cdot Z^{0.77}$	Upper-limit S/Z relationship for vapor-grown crystals	0.7	1.0
Matrosov (2007)	-	$S=0.056 \cdot Z^{1.2}$	Aggregates	1.4	8.5 [b]
Surussavadee and Staelin (2007) and Kulie and Bennartz (2009)	SSKB	$S=0.52 \cdot Z^{0.83}$	Spherical snow particles with density = 200 kg m^{-3}	0.3	0.2 [c]
Pokharel and Vali (2011)	PV11	$S=0.39 \cdot Z^{0.58}$	Rimed snow particles assuming the lower of two density-size relationships	0.3	0.0 [d]
Falconi et al. (2018)	-	$S=0.060 \cdot Z^{1.4}$	Snow particles classified as heavily rimed	0.6 [e]	8.5

140

141 [a] Minimum relative S difference is defined as the minimum of $|(S_{HP}-S)|/S$ where S_{HP} is a measurement of undercatch-corrected liquid-equivalent
142 snowfall rate (Table 6) and S is a snowfall rate on an S/Z relationship line evaluated at one of the attenuation-corrected reflectivities (Sect. 4).

143 [b] Attenuation-corrected Z on this day (0.6 mm^6 m^{-3}) is smaller than the lower-limit Z (1 mm^6 m^{-3}) advised for this S/Z relationship (Matrosov
144 2007).

145 [c] Maximum relative S difference on this day is 0.4.

146 [d] Maximum relative S difference on this day is 0.7.

147 [e] Maximum relative S difference on this day is 0.9.

148

149 **2 - Site, Aircraft, and Instruments**

150 **2.1 - Site**

151   Analyzed herein are aircraft and ground data from 14/15 December 2016 and from 3

152 January 2017. The ground data were acquired in a forest/prairie ecotone on the eastern slope of

153 the Medicine Bow Mountains in southeast Wyoming (Figs. 1a-b). No ground-based observers

154 were deployed during the two snowfall events analyzed.

155   At one of three ground sites (HP in Figs. 1a-b) a hotplate precipitation gauge (Rasmussen

156 et al. 2011; Zelasko et al. 2018), a GPS receiver, and a data acquisition system were deployed.

157 Once per second, the data system ingested a hotplate-generated data string, combined that with

158 time-of-day from the GPS receiver [Coordinated Universal Time (UTC)], and recorded the

159 merged hotplate/UTC data string. The absolute accuracy of the time stamp is no worse than 2 s.

160   Overflights of the hotplate were done by the University of Wyoming King Air (WKA) on

161 14/15 December 2016 and on 3 January 2017. The flights were conducted in preparation for the

162 SNOWIE field project (Tessendorf et al. 2019) and were flown from the Laramie, WY Airport

163 (LA in Fig. 1a). Data acquisition on the WKA was also synchronized with UTC, but with much

164 better accuracy than at the hotplate.

165

166   Measurements of horizontal wind (speed and direction), temperature, relative humidity,

167 and pressure from the US-GLE AmeriFlux tower (AF in Figs. 1a-b) are also components the

168 analysis. The AmeriFlux data were provided to us as 30-minute averages (AmeriFlux 2021;

169 Marlow et al. 2023).

170
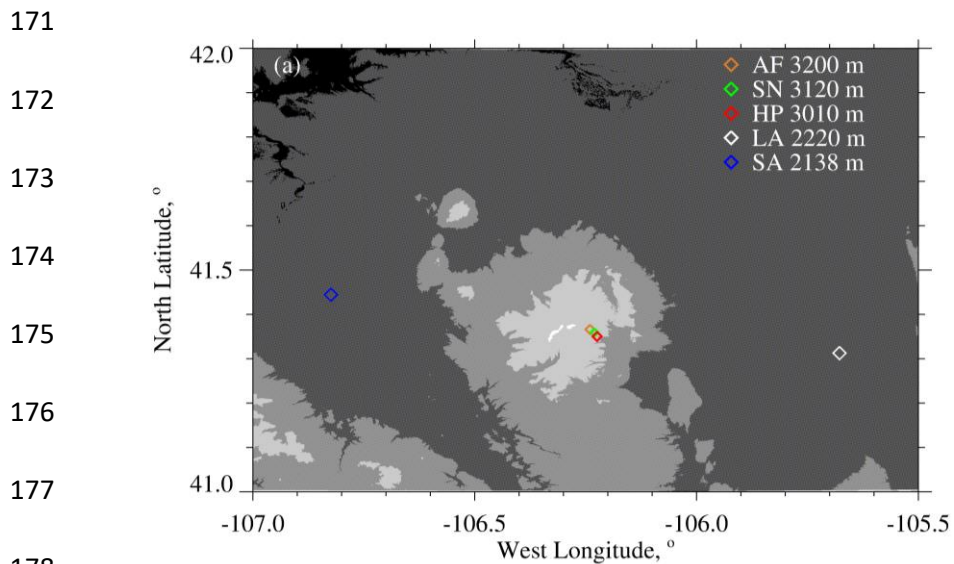
Figure 1 – (a) Southeast Wyoming, airport at Saratoga, WY (SA), airport at Laramie, WY (LA),

and the ground sites: AF = US-GLE AmeriFlux tower, SN = Brooklyn Lake SNOTEL, and HP =

hotplate. Altitudes of the airports and ground sites are in the legend. Altitude thresholds for the

digital elevation map are 1500, 2000, 2500, 3000, and 3500 meters. (b) Close up of the AF, SN,

and HP ground sites (from © Google Earth).

2.2 - University of Wyoming King Air (WKA)

The following WKA measurements were analyzed: aircraft position, temperature, snow particle imagery, and three moments of the cloud droplet size distribution function. A Cloud Droplet Probe (CDP; Faber et al. 2018) was the basis for the droplet size distribution measurements and the derived moments. The latter are droplet concentration (N), cloud liquid water content (LWC), and mean droplet diameter (<D>). Snow particle imagery was obtained using a precipitation particle imaging probe (2DP; Korolev et al. 2011) and a cloud particle imaging probe (2DS; Lawson et al. 2006). These acquired two-dimensional images of particles between 200 to 6400 μm (2DP) and between 10 to 1280 μm (2DS).

2.3 – The W-band Wyoming Cloud Radar (WCR)

Retrievals from the up-looking and down-looking antennas of the WCR, operated on the WKA, were also analyzed. For this we used Level 2 WCR data[2] with reflectivities recorded as $dBZ = 10 \cdot \log_{10}(Z)$. The reflectivities were converted from dBZ to Z prior to processing. Additionally, values of the vertical-component Doppler velocity retrieved from below the WKA using the WCR's down-looking antenna were analyzed. The Doppler velocities were corrected for aircraft motion as described in Haimov and Rodi (2013). We use V_D to symbolize the corrected vertical-component Doppler velocity and adopt the convention that $V_D > 0$ indicates upward hydrometeor motion.

---

[2] http://flights.uwyo.edu/uwka/wcr/projects/snowie17/PROCESSED_DATA/

212   The Level 2 WCR sampling was different on the two flight days and this difference is

213 shown in Table 2. Ground-based calibrations of the WCR's up-looking antenna and correlations

214 between in-flight retrievals acquired using the WCR's up-looking and down-looking antennas

215 were used to estimate the precision and absolute accuracy of the WCR-derived values of dBZ.

216 These are $\pm$ 1.0 dBZ and $\pm$ 2.5 dBZ, respectively (PV11).

217

218   Table 2 – Level 2 WCR sampling and the WKA overflight time

219

Date	Level 2 WCR Vertical Sampling, m	Level 2 WCR Along-track Sampling, s	Overflight Time, UTC
14/15 December 2016	23	0.23	00:00:38 (15 December 2016)
3 January 2017	30	0.36	20:32:03

220
221

222 **2.4 - Hotplate Gauge**

223   Algorithms used to process hotplate measurements are described in Rasmussen et al.

224 (2011), Boudala et al. (2014), and Zelasko et al. (2018). Henceforth, these are referred to as R11,

225 B14, and Z18, respectively. This section describes how hotplate measurements acquired at the

226 HP site were analyzed. The hotplate deployed at the HP site is described in Wolfe and Snider

227 (2012), Z18, and in Marlow et al. (2023).

228   Five measurements fundamental to the steady state energy budget of the hotplate's

229 temperature-controlled up-viewing plate are output by the hotplate microprocessor as one-minute

230 running averages (Z18). These averages were merged with the GPS time and recorded at 1 Hz by

231 the data acquisition system (Sect. 2.1). With these measurements, calibration data (Marlow et al.

232 2023), and the algorithm developed by Z18, we calculated S in two steps. First, the five hotplate

233 measurements (electrical power supplied to the plate, ambient temperature, wind speed,

234 downwelling shortwave flux, and downwelling longwave flux) were input to Eq. 3 in Z18. The

235 output of that equation is a provisional liquid-equivalent precipitation rate. Second, the snow

236 particle catch efficiency, described in the next paragraph, was used to calculate S as the ratio of

237 the provisional rate and the catch efficiency.

238   Marlow et al. (2023; their Fig. 3b) report the relationship between snow particle catch

239 efficiency and wind speed that was applied in the calculation of S. There are three bases for this

240 relationship. First is the catch efficiencies R11 derived using measurements obtained from a

241 weighing gauge, operated within a double fence intercomparison reference shield, and collocated

242 measurements from an unshielded hotplate gauge. These paired measurements are symbolized

243 SRG (shielded reference gauge) and UHG (unshielded hotplate gauge). R11 plotted hotplate

244 catch efficiencies (i.e., UHG/SRG) versus wind speeds measured at 10 m AGL (their Fig. 8).

245 Second is Marlow et al.'s adjustment of R11's 10 m AGL wind speeds to 2 m AGL. The basis

246 for the adjustment is surface boundary layer parameters derived for R11's site (Kochendorfer et

247 al. 2018) and an equation from Panofsky and Dutton (1984; their Eq. 6.7). The adjustment was

248 made because the hotplate-derived wind speeds, both here and in Marlow et al. (2023), were

249 acquired at approximately 2 m above the snowpack surface. Third is Marlow et al.'s comparison

250 of SNOTEL-derived liquid-equivalent depth changes and hotplate-derived time-integrated

251 accumulations. The interval for the comparisons is 24 hours. Based on the comparison, which

252 has 57 paired values acquired at the sites labeled HP and SN in Fig. 1, the average fractional

253 absolute relative difference is 0.30. Marlow et al. also provided an estimate of the error in a

254 SNOTEL measurement (2.4 mm). At accumulation = 10 mm the error corresponds to a relative

255 error = 0.24. This indicates that SNOTEL contributed significantly to the SNOTEL/hotplate

256 variance and especially so for the smaller accumulations in Fig. 9a of Marlow et al. (2023).

257 Because of this, we do not limit the following estimate of hotplate precision to a subset of the 57

258 paired measurements. Based on our assessment of the average fractional absolute relative

259 difference, the hotplate precision applied in this analysis was taken to be 0.3.

260   The hotplate-derived wind speeds acquired at ~ 2 m, and discussed in the previous

261 paragraph, are henceforth symbolized U_{PRO}. The basis for these is a steady state energy budget of

262 the hotplate's temperature-controlled down-viewing plate and a proprietary algorithm (R11 and

263 Z18). The U_{PRO} are reported by a hotplate as one-minute running averages (Z18) and we

264 recorded these at 1 Hz. Examples are the gray dots in Fig. 2. Additionally, we calculated and

265 analyzed one-minute-averaged values of U_{PRO} and the corresponding standard deviations.

266 Examples of these are the black circles and the short vertical line segments in Fig. 2.

267

268

269

270

271

272

273
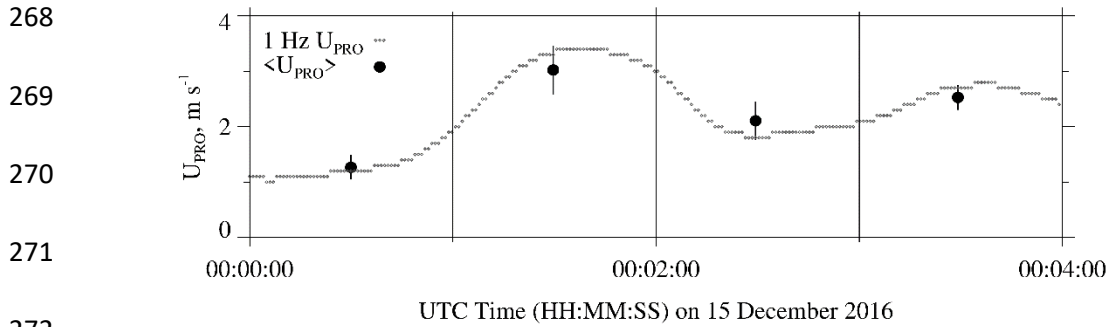
274   Figure 2 – Hotplate wind speed measurements (U_{PRO}) 00:00:00 to 00:04:00 on 15 December

275   2016. Gray dots are the one-minute running-average U_{PRO} recorded at 1 Hz. Black circles are the

276   one-minute-averaged U_{PRO} ($\pm$ 1 standard deviation).

277

278 **3 - Analysis**

279 **3.1 - WKA Overflight Time**

280   The focus of our analysis is the two WKA flight segments shown in Figs. 3a-b. The maps

281 shown in the figures have the three ground sites (AF, SN, and HP) and the WKA flight tracks

282 (white line). The beginning-to-end time interval for the flight tracks is 100 s and these are

283 divided into ten 10-second intervals. The 10 s intervals are indicated with white diamonds.

284 Except for the turn evident in Fig. 3b, the flight tracks are straight, and the track direction is

285 approximately upwind to downwind.

286   Times that the WKA was closest to the HP site were evaluated by finding the point on the

287 flight track where the horizontal position of the WKA was closest to the hotplate's coordinates.

288 These times are symbolized t_0 and are referred to as overflight times. In Figs. 3a-b the downwind

289 end of the flight tracks end at the overflight time. The latitude/longitude position of the aircraft

290 was within 390 m of the hotplate at the overflight times. Table 2 has the overflight times on the

291 two flight days.

292

293

294

295

296

297

298

299
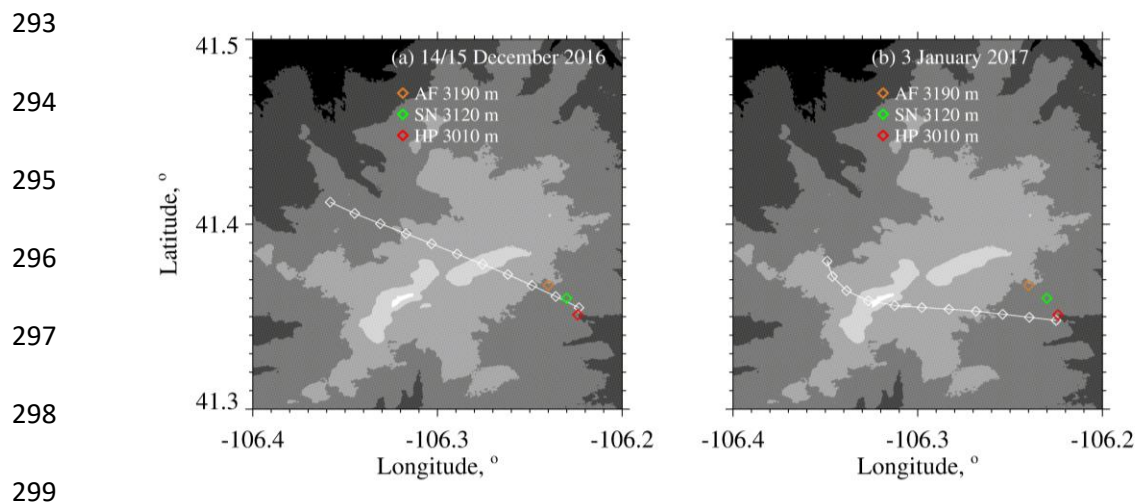
Figure 3 – (a) WKA flight track on 14/15 December 2016 for time interval = overflight time -

100 s to the overflight time. (b) WKA flight track on 3 January 2017 for time interval =

overflight time - 100 s to the overflight time. The white diamonds on the tracks are separated, in

time, by 10 s. Altitude thresholds for the digital elevation maps are 2600, 2800, 3000, 3200,

3400, and 3600 meters. Altitudes of the ground sites are in the legend.

305

3.2 – Effect of Attenuation on WCR Reflectivities

The presence of molecular oxygen, water vapor, cloud water, and snow particles within the WCR's transmission path will contribute to an attenuation of microwave intensity and will therefore negatively bias the retrieved reflectivities (Matrosov 2007; Hiley et al. 2011; Kneifel et al. 2015). Models of attenuation, radar remote sensing, and in situ measurements were used to calculate this bias. For oxygen, an attenuation coefficient from Ulaby et al. (1981; their Fig. 5.6), and temperature (T) and pressure (P) measurements from the AF (Table 3), were used. For vapor, an attenuation coefficient (Ulaby et al. 1981; their Eq. 5.22), and T, P, and relative humidity (RH) measurements from the AF (Table 3), were used. Concentrations of oxygen and water vapor and the oxygen and vapor path lengths are provided in Table 4. The latter is the vertical distance between the HP and the WKA. It was assumed that concentrations were uniform over this path length.

Attenuation by cloud water was derived using the WKA-measured T (Table 3), the WKA-measured LWC, path length (Table 4), and an attenuation formula (Liebe et al. 1989; Vali and Haimov 2001). The LWC applied in the formula is the maximum of CDP measurements acquired between t_0 - 10 s and t_0. This interval coincides with the interval the WCR's down-looking antenna was used to acquire reflectivities over the HP (Sect. 3.5). The path length for cloud water was derived as the vertical distance between cloud base [derived thermodynamically using AF measurements (Table 3)] and flight level. LWC was assumed uniform, at the maximum value, over the path length.

Snow particle mass concentration is typically reported as an ice water content (IWC, g m^{-3}) (Liu and Illingworth 2000). The contribution of IWC to attenuation was calculated using

329   measurements in Nemarich et. al (1988), who reported an attenuation coefficient equal to 0.9

330   dB/km per unit of IWC. Also used were retrievals of IWC acquired using the down-pointing

331   WCR antenna. There are several steps in the calculation. First, all profiles of dBZ acquired

332   between t_0 - 10 s and t_0 were selected. Second, a maximum dBZ was selected at each of the

333   down-beam range gates (Table 2). Third, the dBZ maxima were increased by the overall two-

334   way attenuation in the final column of Table 4. Fourth, the profile of attenuation-corrected dBZ

335   was converted to a profile of attenuation-corrected Z. Fifth, a Z-to-IWC parameterization was

336   applied (IWC = $0.10 \cdot Z^{0.51}$; PV11; their Table 3). Sixth, the IWC profile was integrated, and the

337   derived ice water path was divided by the snow particle path length (Table 4). This calculation

338   produced a time- and range-averaged maximum IWC (Table 4). This IWC is the value applied in

339   the attenuation calculation.

340   Two-way attenuations (ΔdB), summed over contributions from the four components, are

341   presented in the final column of Table 4. Attenuation by snow and attenuation by liquid were the

342   most important components (> 50 %) on December 15 and January 3, respectively. Vapor

343   contributed 32 % to the overall on December 15, and the combination of vapor and snow

344   contributed 45 % on January 3. Equation 1 shows how an attenuation-corrected reflectivity (Z')

345   was derived using an uncorrected reflectivity (Z) and the ΔdB .

346

347    $$Z' = 10^{\left[\left[10 \cdot \log_{10}(Z) + \Delta dB\right]/10\right]} \qquad\qquad (1)$$

348   Table 3 – Atmospheric state averages

349

Date	WKA [a] Track Altitude, m	WKA [a] T, °C	AF [b] T, °C	AF [b] RH, %	WKA [a, c] Track Vector	WKA [a, c] Wind Vector	AF [b, c] Wind Vector
14/15 December 2016	4546	-13.9	-6.3	86	310 / 130	274 / 32	250 / 8.5
3 January 2017	4196	-21.7	-14.6	77	280 / 120	265 / 27	260 / 5.4

350
351

352   [a] Altitude, temperature, track vector, and horizontal wind vector data obtained by averaging 1 Hz

353   WKA measurements. The averaging interval is 60 s and the interval starts at the overflight time,

354   minus 60 s, and ends at the overflight time.

355

356   [b] Temperature (T), relative humidity (RH), and horizontal wind vector data from sensors on the

357   US-GLE AmeriFlux tower (Sect. 2.1). The wind sensor was deployed at 26 m AGL (3223 m

358   MSL) and the T/RH sensor was deployed at 23 m AGL (3220 m MSL). The AF measurements

359   correspond to 30-minute averages closest to the overpass time. In the AF data set, time stamps on

360   the relevant AF recordings are 00:00 UTC (15 December 2016) and 20:30 UTC (3 January

361   2017).

362

363   [c] Vectors are presented in the following format: Direction of motion (degree relative to true

364   north) / speed (m s^{-1}).

365   Table 4 – Attenuating component concentration, one-way pathlength, and the overall two-way attenuation

Date	Conc. Oxygen, kg m^{-3}	Conc. Vapor, kg m^{-3}	Maximum LWC, g m^{-3}	Maximum IWC, g m^{-3}	One-way Pathlength [a] Oxygen, Vapor, and Snow, km	One-way Pathlength [b] Cloud Water, km	Overall Two-way Attenuation, ΔdB
15 December 2016	0.21	2.7x10^{-3}	0.01	0.27	1.54	1.09	1.41 [c]
3 January 2017	0.21	1.3x10^{-3}	0.08	0.09	1.19	0.59	1.01 [d]

366

367   [a] Vertical distance between HP and WKA

368

369   [b] Vertical distance between cloud base [derived thermodynamically using AF measurements (Table 3)] and WKA

370

371   [c] One-way attenuation coefficients are 0.03 dB/km for oxygen (Ulaby et al. 1981), 0.14 dB/km for vapor (Ulaby et al. 1981), 0.056

372   dB/km for cloud water (Liebe et al. 1989; Vali and Haimov 2001), and 0.24 dB/km for snow particles (Nemarich et. al 1988).

373

374   [d] One-way attenuation coefficients are 0.03 dB/km for oxygen (Ulaby et al. 1981), 0.073 dB/km for vapor (Ulaby et al. 1981), 0.49

375   dB/km for cloud water (Liebe et al. 1989; Vali and Haimov 2001), and 0.077 dB/km for snow particles (Nemarich et. al 1988).

376

377 **3.3 - Correction of Doppler Velocity**

378 We accounted for bias in V_D (Sect. 2.3) due to deviation of the down-looking WCR

379 antenna from vertical. This was done by applying the correction described in Zaremba et al.

380 (2022) (their Eq. A4). The west-to-east and south-to-north particle velocities used in the

381 correction were assumed to be equal to component wind velocities. The latter were expressed as

382 linear functions of altitude using the information in the penultimate and last columns of Table 3.

383 The component velocities as functions of altitude and the linear equations relating velocity and

384 altitude are provided in the Appendix.

385 **3.4 - Hotplate Measurement of Wind Speed**

386 Here we compare the hotplate-derived wind speed to wind speed derived using an

387 R.M.Young rotating anemometer (R.M.Young 2001). The second of these is symbolized U_{RMY}

388 and the basis for the first (U_{PRO}) is a proprietary algorithm (Sect. 2.4). We are doing this

389 comparison because B14 showed that U_{PRO} can be high-biased, relative to a conventional

390 anemometer, and because U_{PRO} is the primary determinant of the rate that the up-viewing plate

391 dissipates sensible heat energy. Diagnosis of that heat transfer rate is our basis for calculating the

392 liquid-equivalent snowfall rate (Z18). The U_{PRO} also determines the snow particle catch

393 efficiency and the latter was used in calculations of the undercatch-corrected liquid-equivalent

394 snowfall rate (Sect. 2.4).

395 The comparisons reported here were done at the Laramie, WY Airport in December

396 2019, and in January 2020. Compared to the HP site, the Laramie Airport site (indicated LA in

397 Fig. 1) is free of obstruction, out to 120 m, and experiences larger wind speeds. By mounting the

398 hotplate and the R.M.Young anemometer on rigid metal pipes, the hotplate's heated horizontal

399   surfaces (the up- and down-viewing plates seen in Fig. 1 of Z18) and the anemometer's spinning

400   axis (oriented horizontally) were both positioned at 2 m AGL. The pipes were separated

401   horizontally by 5 m. There was no precipitation on the days selected for the wind speed

402   comparisons. The values of U_{PRO} and U_{RMY} we analyzed were recorded with a data system that

403   time stamped the 1 Hz U_{PRO} and 1 Hz U_{RMY} with a relative timing accuracy no worse than 1 s.

404   A wind speed comparison - from 13 December 2019 - is shown in Fig. 4a. U_{PRO} was

405   brought into the comparison by sampling it once per minute from files containing 1 Hz

406   recordings of the one-minute running-average U_{PRO} (Sect. 2.4). U_{RMY} was brought into the

407   comparison by starting with files containing 1 Hz recordings and converting these to one-minute

408   averages. Fig. 4a shows no evidence of bias and Fig. 4b demonstrates that the average absolute

409   departure between the U_{PRO} and U_{RMY} (both one-minute averages) is no larger than 1 m s^{-1}. Table

410   5 has eight more precipitation-free comparisons. Included in the table are temperature and wind

411   speed averaged over the comparison intervals (4 to 20 UTC), the slope of the linear-least-squares

412   fit line (forced through the origin, red line), and the lower and upper quartiles of the slope. The

413   quartiles were calculated using the method of Wolfe and Snider (2012). In contrast to Figs. 4a-b,

414   Figs. 4c-d make the comparison using 1 Hz values of U_{PRO} and U_{RMY}. The larger scatter and

415   larger average absolute departure seen in these panels is a consequence of the hotplate's limited

416   time response, compared to the R.M.Young. We quantify the hotplate's response time in terms of

417   a calculated thermal response time. During wintertime at the Laramie Airport, and with wind

418   speed at 5 m s^{-1}, the down-viewing plate's thermal response time is approximately 60 s (results

419   not shown). Because the temperature of the down-viewing plate is actively controlled, this does

420   not translate to a 60 s lag between changes in wind speed and the hotplate response. The

421   U_{PRO}/U_{RMY} departure is most evident at $U_{PRO} > 5$ m s^{-1} (Fig. 4d) but this is not a concern for

422 U$_{PRO}$ on 14/15 December 2016 or on 3 January 2017. Snider (2023) demonstrated that the U$_{PRO}$

423 was less than 5 m s^{-1} at the hotplate during the two WKA overflights.

424

431
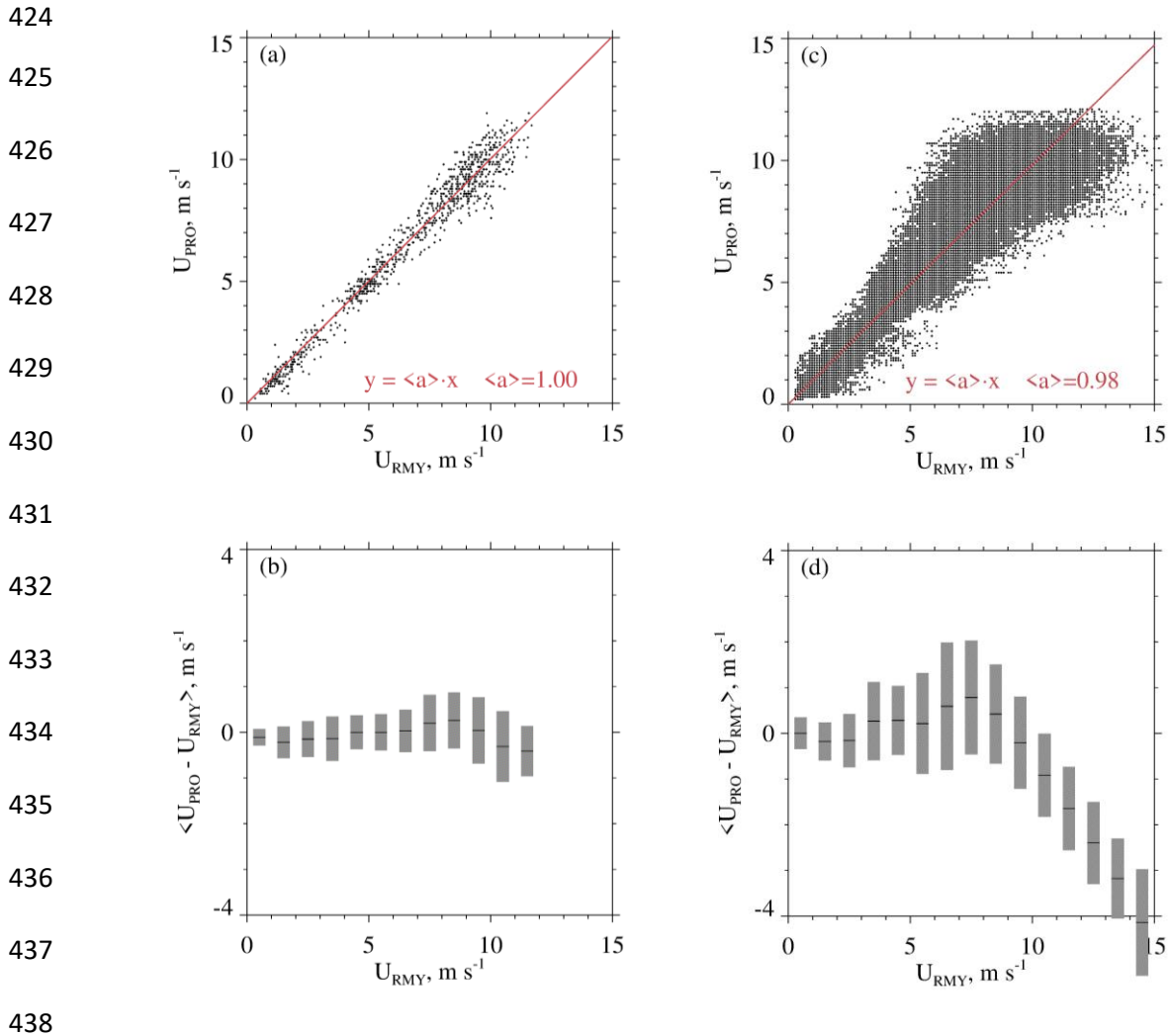
Figure 4 – (a) Scatterplot of one-minute-averaged U_{PRO} and one-minute-averaged U_{RMY}.

Measurements were acquired at the Laramie, WY Airport 13 December 2019. The red line is a

linear-least-squares fit line (forced through the origin). (b) Average departure between one-

minute-averaged U_{PRO} and one-minute-averaged U_{RMY}. Average departures were calculated for

discrete U_{RMY} intervals, and the averages are indicated with short black horizontal lines. Gray

bars indicate $\pm$ 1 standard deviation. (c) Same as in (a) except for 1 Hz values of U_{PRO} and U_{RMY}.

(d) Same as in (b) except for 1 Hz values of U_{PRO} and U_{RMY}.

447

448   Table 5 - U_{PRO} versus U_{RMY} correlations

449

Date, UTC [1]	$\langle T \rangle$ [2], °C	$\langle U \rangle$ [2], m s^{-1}	$\langle a \rangle$ [3]	a [4] First Quartile	a [4] Third Quartile
7 December 2019	-0.40	5.40	1.00	0.90	1.04
8 December 2019	2.70	4.10	0.99	0.90	1.04
10 December 2019	-5.20	3.80	0.99	0.83	1.04
13 December 2019	-1.50	6.60	1.00	0.93	1.06
18 December 2019	-6.20	3.60	0.99	0.92	1.04
19 December 2019	-6.90	2.70	0.95	0.84	0.99
6 January 2020	-6.40	8.80	1.01	0.96	1.06
8 January 2020	0.30	4.20	1.00	0.87	1.05
11 January 2020	-7.20	7.00	1.02	0.97	1.08

450

451

452   [1] Statistics presented are based on one-minute-averaged U_{PRO} and one-minute-averaged U_{RMY}

453   measurements made between 04:00 to 20:00 UTC.

454

455   [2] Interval-averaged temperature and interval-averaged wind speed.

456

457   [3] Slope of the one-minute-averaged U_{PRO} versus one-minute-averaged U_{RMY} linear-least-squares

458   fit line, forced through the origin.

459

460   [4] Quartiles of the slope (see text)

461

3.5 – Combined Aircraft and Surface Measurements

Figure 5 has WCR and WKA measurements starting 100 s prior to t_0 and ending at t_0. The sequences in Figs. 5a and 5c are reflectivities from both the up- and down-looking antennas. In Fig. 5a the flight track (black dashed horizontal line) is at 4550 m and in Fig. 5c the flight track is at 4200 m. At the t_0 in Fig. 5a, below the WKA, the maximum radar echo is +6 dBZ ($Z = 4$ mm^6 m^{-3}) and in Fig. 5c the maximum is -3 dBZ ($Z = 0.5$ mm^6 m^{-3}). Supercooled liquid water was detected as the aircraft approached the ridgeline (Fig. 5b) and during the last 10 seconds of the time sequence in Fig. 5d. During these encounters with supercooled liquid, the maximum LWC values were 0.03x10^{-3} and 0.08x10^{-3} kg m^{-3} on 14 December 2016 and 3 January 2017, respectively. Values of N (Sect. 2.2) at times of maximal LWC were 3x10^6 and 100x10^6 m^{-3} on 14 December 2016 and 3 January 2017, respectively. Even on 3 January 2017, the <D> (Sect. 2.2) associated with maximum LWC was sufficient for hexagonal plate crystals with diameter larger than 100 µm to collide with the observed droplets with efficiencies > 0.1 (Wang and Ji 2000).

We temporally and spatially averaged the values of Z we compared with time-averaged values of S. There are two reasons for this: 1) As discussed in Sect. 3.1, the WCR did not sample Z exactly over the hotplate, and furthermore, the width of radar beam at 1500 m range - roughly the distance between the aircraft and the ground at the overflight times - is 30 m and thus considerably smaller than the minimum horizontal distance between the aircraft and the HP. 2) Compared to the WCR, the hotplate is a relatively slow-response measurement system whose output is commonly averaged over one-minute intervals (Z18).
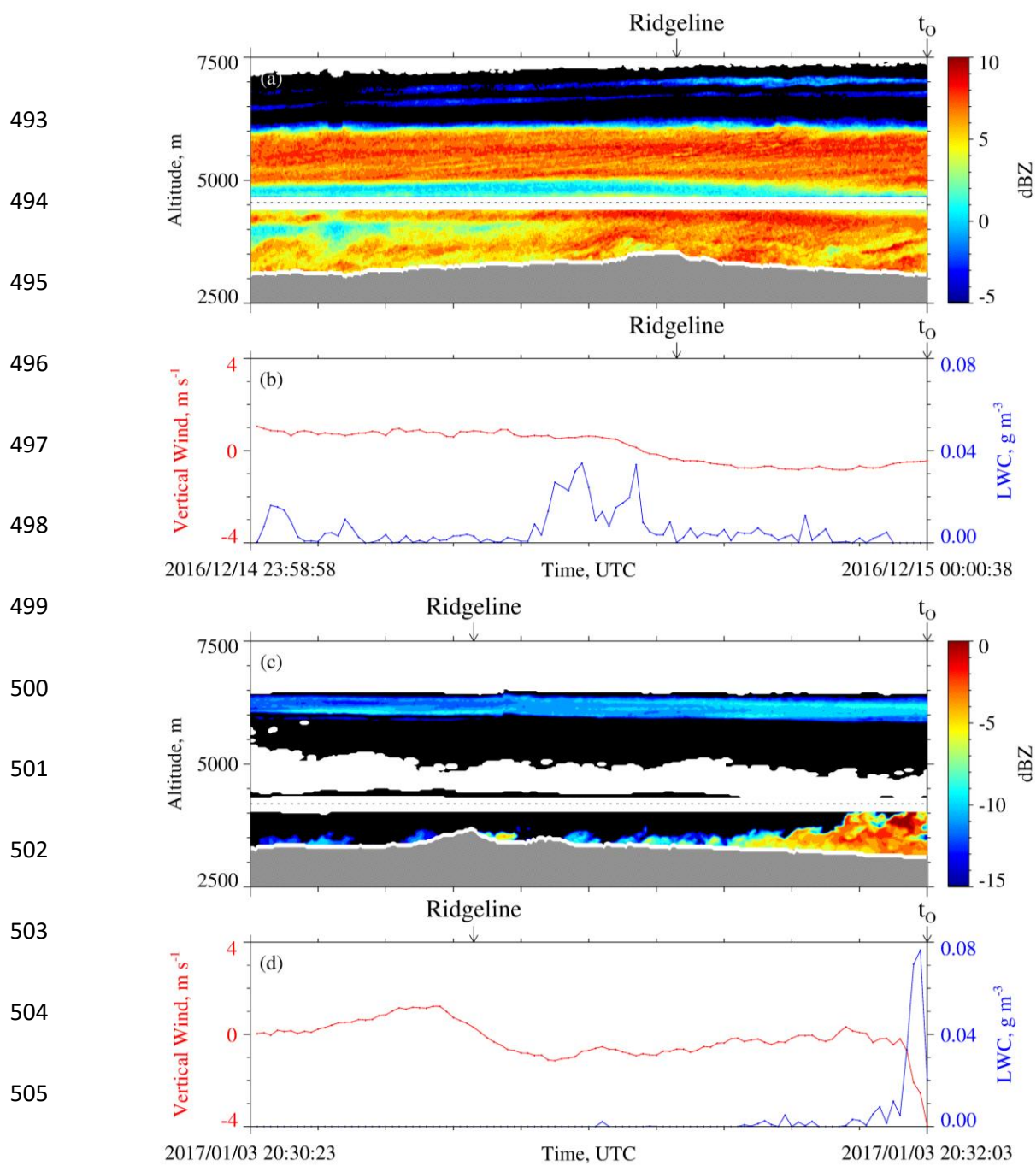
484   FIGURE 5 WAS REVISED IN REVISION3.

485

486

487

488

489

490

491

492

Figure 5 – (a) 100 s of WCR reflectivity and (b) 100 s of LWC and gust probe vertical

wind velocity ending at t_0 on 14/15 December 2016. (c) 100 s of WCR reflectivity and (d) 100 s

of LWC and gust probe vertical wind velocity ending at t_0 on 3 January 2017. In (a) and (c),

above and below the flight track, the roughly 200-m-deep WCR blind zone is evident,

reflectivity above (below) the flight track is from the up-looking (down-looking) WCR antenna,

512 black indicates dBZ values smaller than the minimum indicated in the color bar, white

513 immediately above the terrain indicates echo that was discarded because of ground clutter, and

514 white above the ground clutter and outside of the blind zone indicate dBZ < minimum detectable

515 signal.

516   In our analysis, the HP measurements were averaged over two adjacent 60 s intervals.

517 The first extends from t_0 to $t_0 + 60$ s (Fig. 6a) and the second from $t_0 + 60$ s to $t_0 + 120$ s (Fig.

518 6c). In Fig. 6a and in Fig. 6c, $t_{HP,B}$ symbolizes an interval's beginning time and $t_{HP,E}$ symbolizes

519 an interval's ending time. Formulas describing how these times were related to the beginning and

520 ending time of a corresponding WCR averaging interval are in the Appendix. Fig. 6b is a

521 schematic of the first WCR averaging interval and Fig. 6d is a schematic of the second. Again,

522 the subscripts "B" and "E" are used to indicate averaging beginning and ending times. Figures 6b

523 and 6d both have lines at the top of an averaging interval/domain. The slopes of these lines are

524 proportional to the ratio of two speeds. These speeds are a maximum likely snow particle speed

525 toward the ground (v_p) and a horizontal wind advection speed (v_w). The v_p was calculated

526 using averaged vertical-component Doppler velocities and v_w was calculated using a vertical

527 profile of horizontal winds, based on WKA horizontal wind measurements and AF horizontal

528 wind measurements (Figs. A1a-b), and using the WKA track vector (Table 3). An altitude ($z' =$

529 3400 m) was assumed in the calculation of v_w. This is the altitude of the ridges west and

530 northwest of the HP site (Figs. 3a-b). Picking the altitude to be either $z' = 3200$ m or $z' = 3600$ m
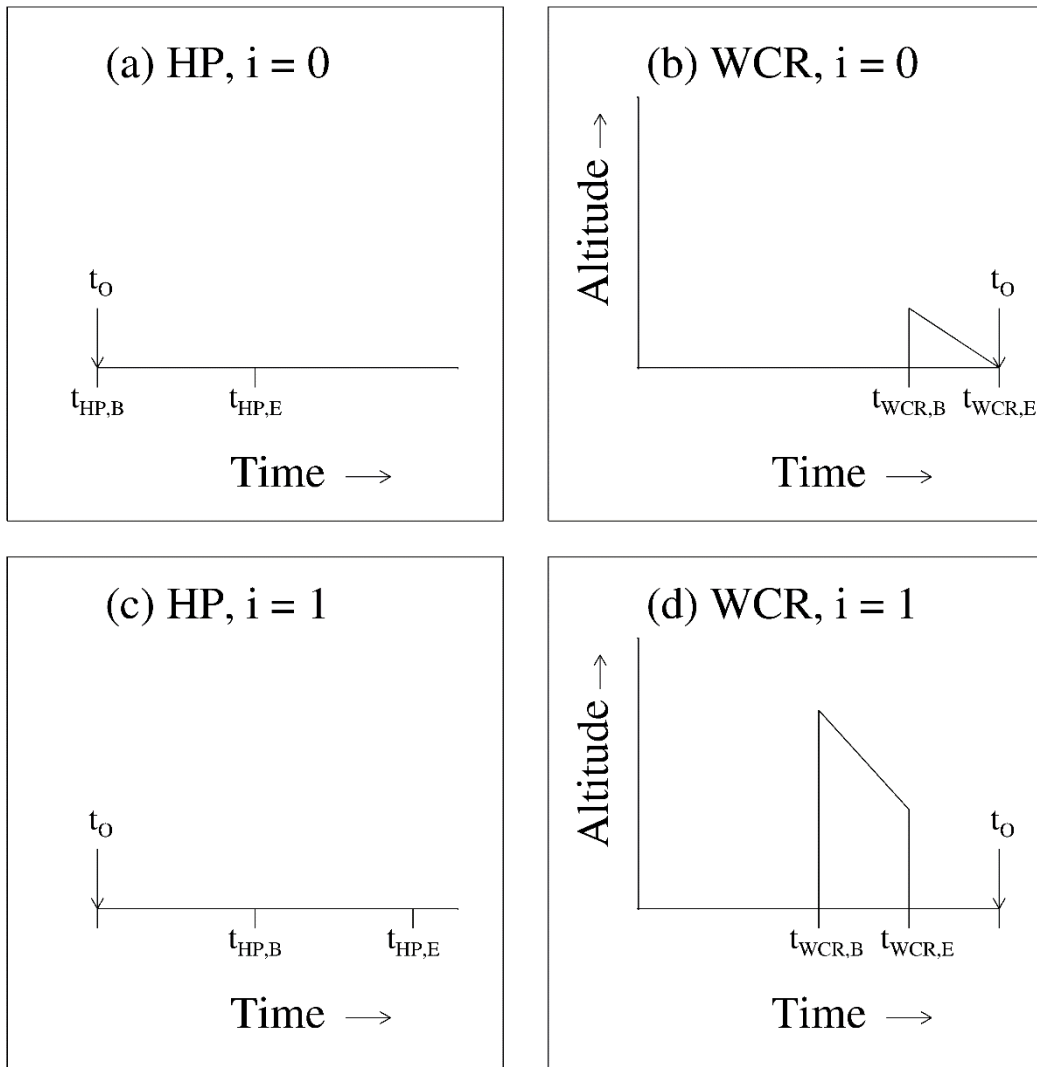
531 does not alter our findings.

532

Figure 6 – (a and c) Representations of the $i = 0$ and $i = 1$ HP averaging intervals. (b and d)

Representations of the $i = 0$ and $i = 1$ WCR averaging intervals/domains. The t_0 is shown in all

panels. The subscripts "B" and "E" indicate beginning and ending times of the HP averaging

(panels a and c) and the beginning and ending times of the WCR averaging (panels b and d).

558

559   All panels in Fig. 6 are labeled with an index designating either the first averaging

560 interval ($i = 0$) or the second averaging interval ($i = 1$). Figures 7 and 8 present hotplate

561 snowfall measurements from 14/15 December 2016 and 3 January 2017. In these, and in

562 subsequent figures, colored circles surround the $i = 0$ and $i = 1$ indexes, blue is used to color-

563 code 15 December 2016, and red is used to color-code 3 January 2017. Additionally, Fig. 8 has

564 an $i = 2$ averaging interval. This is a special case discussed at the end of this section.

565   Figures 9a-b and Figs. 10a-b have enlarged views of the altitude-time WCR crossections

566 recorded on the two flight days. Different from Fig. 5a and Fig. 5c, these measurements are only

567 from the WCR's down-looking antenna. Additional differences are the following: 1) The plots

568 are set up so that Z and V_D structures downwind of the hotplate can be seen. These structures are

569 discussed in the following section. 2) The WCR measurements are shown for 50 s of flight. With

570 the WKA ground speed approximately 125 m s^{-1} (Table 3), the distance along the abscissa is

571 6250 m. 3) Colored circles that surround the indexes are placed below the WCR averaging

572 intervals/domains. The latter are drawn with solid black lines and are seen to overlay both the Z

573 and V_D altitude-time crossections. Consistent with Figs. 6b and 6d, and the Appendix, one of

574 these black lines is vertical and another is negatively sloped. Figs. 10a-b also have the $i = 2$

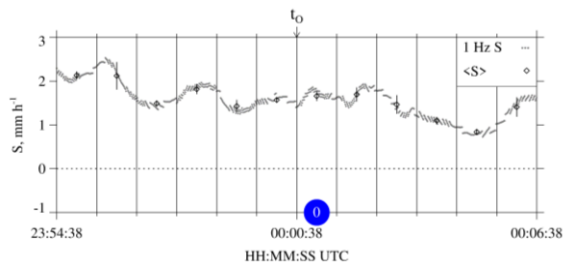575 intervals/domains discussed at the end of this section.

576

577 THIS FIGURE WAS REVISED IN REVISION3.
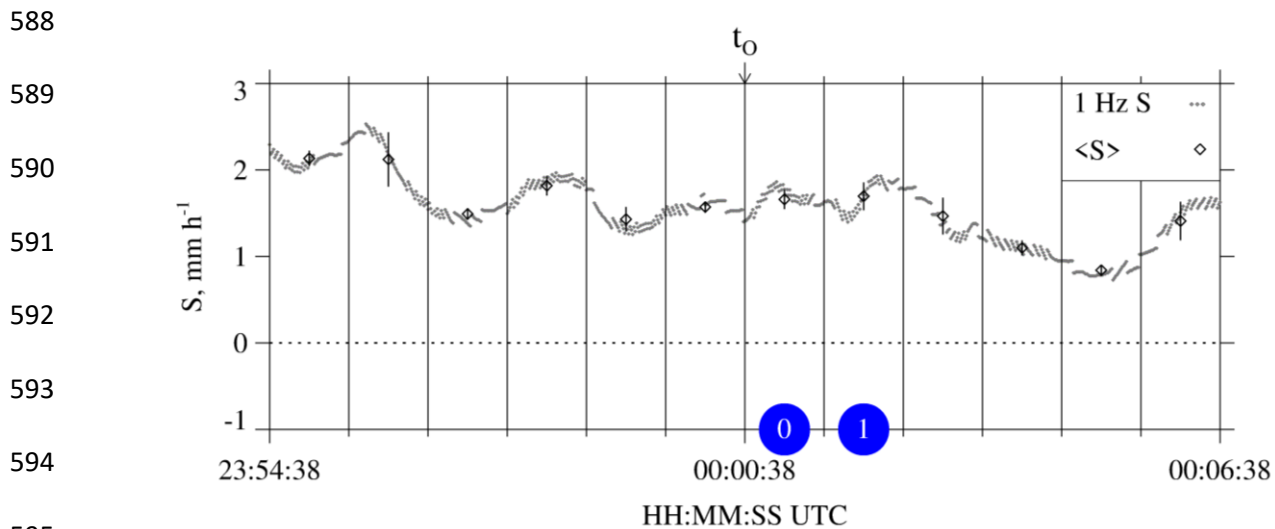
578

579

580

581

582

583

584

585

586

587

588

589

590

591

592

593

594

595

596

597 Figure 7 – Twelve minutes of HP snowfall measurements from 14/15 December 2016. Gray dots

598 are S values calculated using hotplate output recorded at 1 Hz. Black diamonds are the one-

599 minute-averaged values (± 1 standard deviation). The t_0 is shown above the panel and blue

600 circles designate the $i = 0$ and $i = 1$ HP averaging intervals.
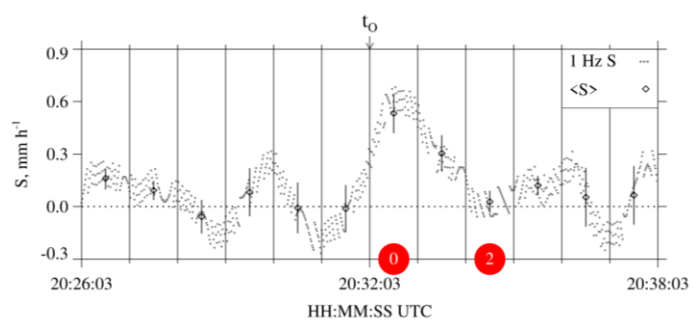
601

602   THIS FIGURE WAS REVISED IN REVISION3.

603

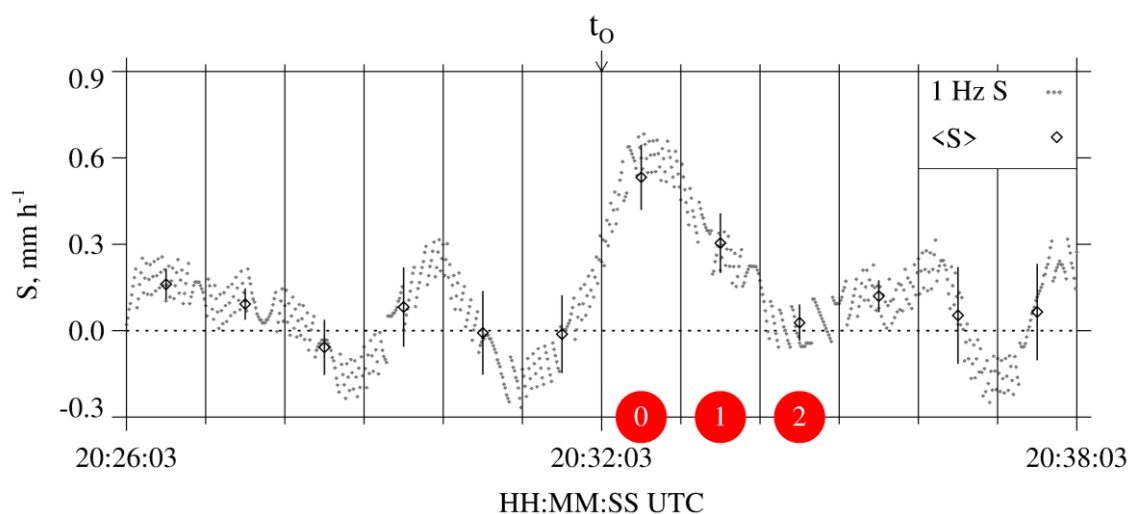604

605

606

607

608

609

610

611

612

613

614

615

616

617

618

619

620 Figure 8 – Twelve minutes of HP snowfall measurements from 3 January 2017. Gray dots are S

621 values calculated using hotplate output recorded at 1 Hz. Black diamonds are the one-minute-

622 averaged values (± 1 standard deviation). The t_0 is shown above the panel and red circles

623 designate the $i = 0$, $i = 1$, and $i = 2$ HP averaging intervals. The $i = 2$ interval is a special case

624 discussed at the end of Sect. 3.5.

625

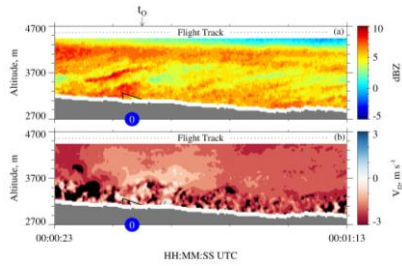626   THIS FIGURE WAS REVISED IN REVISION3.

627

628

629

630

631

632

633
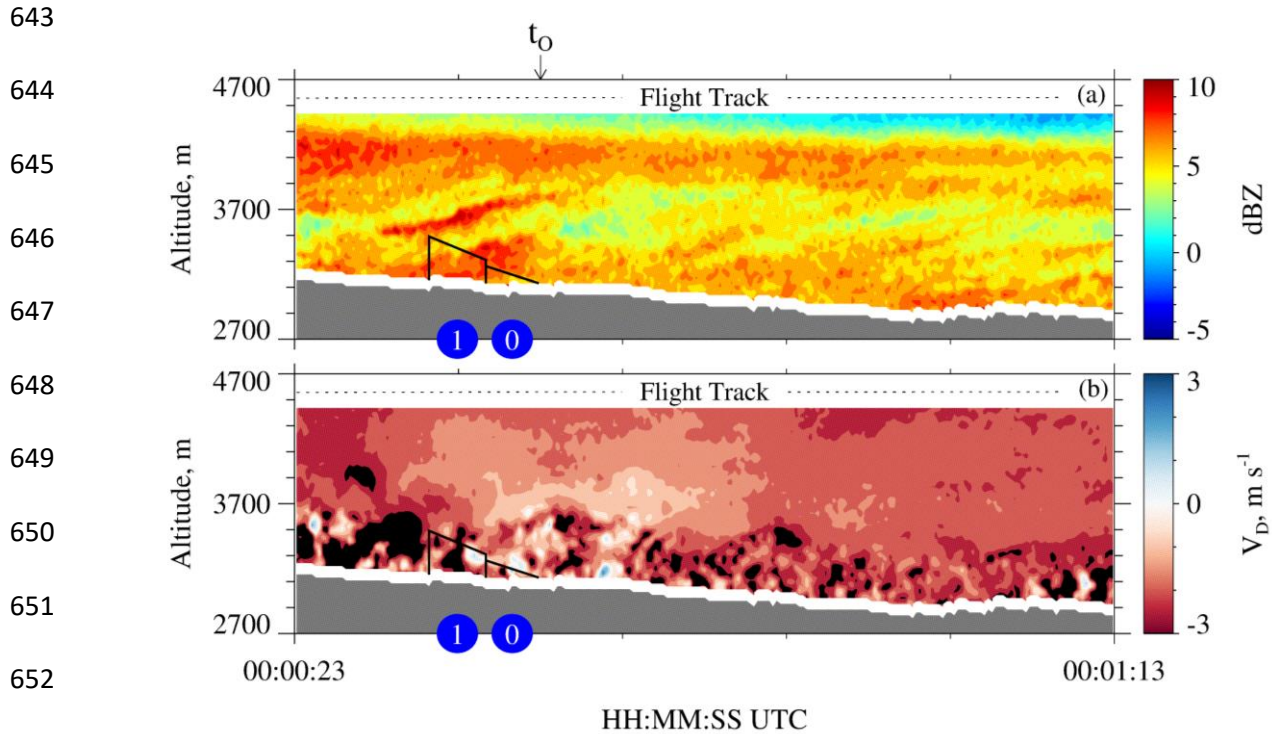
634

635

636

637

638

639

640

641

642

643

655 Figure 9 – 50 s of measurements from the down-looking WCR antenna on 15 December 2016.

656 (a) Crossection of reflectivity t_0 - 15 s to t_0 + 35 s. (b) Crossection of Doppler velocity t_0 - 15 s to

657 t_0 + 35 s. The t_0 is shown above the top panel. In both panels, the solid black lines (vertical and

658 sloped) encompass the $i = 0$ and $i = 1$ WCR averaging intervals/domains and blue circles

659 designate the WCR averaging intervals.

660

661   THIS FIGURE WAS REVISED IN REVISION3.

662

663

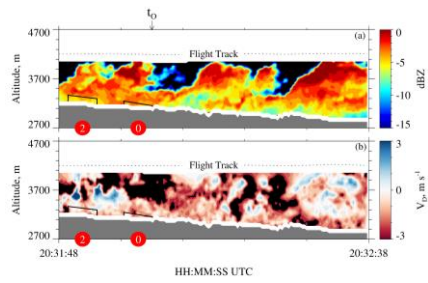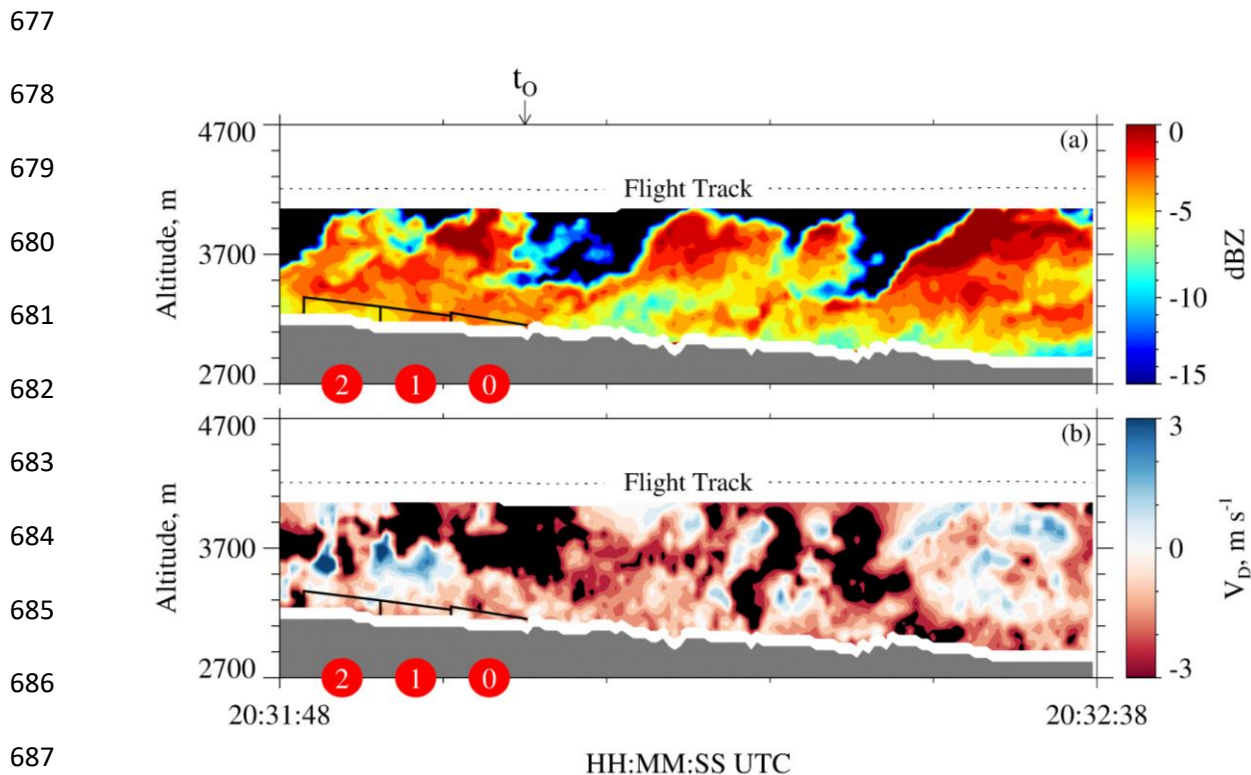HH:MM:SS UTC

677

678

687

688

689

690   Figure 10 – 50 s of measurements from the down-looking WCR antenna on 3 January 2017. (a)

691   Crossection of reflectivity t_0 - 15 s to t_0 + 35 s. (b) Crossection of Doppler velocity t_0 - 15 s to t_0

692   + 35 s. The t_0 is shown above the top panel. In both panels, the solid black lines (vertical and

693   sloped) encompass the $i = 0$, $i = 1$, and $i = 2$ WCR averaging intervals/domains and red circles

694   designate the $i = 0$, $i = 1$, and $i = 2$ WCR averaging intervals/domains. The $i = 2$ interval/domain

695   is a special case discussed at the end of Sect. 3.5.

696

697　　　　The $i=0$ and $i=1$ averages of S and Z are presented in Table 6 and the corresponding

698　averaging intervals are viewable in Fig. 7 and Fig. 9a (15 December 2016) and in Fig. 8 and Fig.

699　10a (3 January 2017). According to the averaging scheme (Fig. 6), the $i=1$ HP averaging

700　interval is time-shifted positively compared to the $i=0$ HP averaging interval and the $i=1$

701　WCR averaging interval is time-shifted negatively compared of the $i=0$ WCR averaging

702　interval. This arrangement of the averaging intervals is one way to average while also accounting

703　for wind advection of the snow particles.

704　　　　As discussed earlier in this section, the averaging scheme initializes with 60-second

705　blocks of HP data between t_o and t_o+120 s. When we applied the scheme to data from 3 January

706　2017, but outside the specified time range, an inconsistency was documented. This is apparent in

707　Fig. 8, where the t_o+120 s to t_o+180 s interval (i.e., the $i=2$ interval) has negligible average S,

708　while in Fig. 10, the $i=2$ interval has a non-negligible average Z (~ 0.3 mm^6 m^{-3}). A firm

709　explanation is not available for the inconsistency, but a factor may be the convective nature of

710　the fields in Figs. 10a-b. Because of the inconsistency, only averages corresponding to the $i=0$

711　and $i=1$ intervals are analyzed further.

712 Table 6 – Average wind measurements, average hotplate measurements, average WCR measurements, and attenuation-corrected

713 reflectivities

Date	v_w [a], m s^{-1}	i index	$S_{HP} \pm \sigma$ [b], mm h^{-1}	WCR Samples [c]	$<V_D>$ [d], m s^{-1}	σ_{V_D} [e], m s^{-1}	v_p [f], m s^{-1}	$<Z> \pm \sigma_Z$ [g], mm^6 m^{-3}	Z' [h], mm^6 m^{-3}
15 December 2016	7.4	0	1.7±0.1	42	-1.3	0.9	2.2	4.9±2.1	6.8
15 December 2016	7.4	1	1.7±0.2	149	-1.8	1.2	3.0	5.6±1.1	7.8
3 January 2017	8.9	0	0.5±0.1	22	-0.9	0.8	1.7	0.49±0.05	0.62
3 January 2017	8.9	1	0.3±0.1	35	-0.8	0.4	1.2	0.50±0.10	0.63

714

715 [a] Horizontal wind advection speed (Eq. A7) calculated using values from the penultimate and last columns of Table 3.

716 [b] One-minute average of the undercatch-corrected liquid-equivalent snowfall rate (± 1 standard deviation). An example averaging

717 interval is the $i = 0$ interval in Fig. 7.

718 [c] Number of samples used to calculate the WCR statistics. The averaging intervals/domains (e.g., $i = 0$ in Figs. 9a-b and in Figs. 10a-

719 b) encompass the WCR samples which are the basis for the WCR statistics presented in this table.

720 [d] Average of Doppler velocity within the averaging intervals/domains.

721 [e] Standard deviation of Doppler velocity within the averaging intervals/domains.

722 [f] Maximum likely snow particle speed toward the ground (Eq. A8).

723 [g] Average reflectivity (± 1 standard deviation). These values are not corrected for attenuation.

724 [h] Attenuation-corrected reflectivities. These were derived using reflectivities from the penultimate column of this table, attenuations

725 from Table 4, and Eq. 1.

3.6 - Snow Particle Imagery

726

727   In Fig. 9a and Fig. 10a, the time for a snow particle to move the abscissa and ordinate

728   distances is different. The ratio of these two times is 2.6. This follows from our choice of

729   abscissa and ordinate ranges, from values of particle fall speed (1 m s^{-1}) and horizontal wind

730   advection speed (8 m s^{-1}), which we assumed, and from the WKA ground speed ($gs \sim 125$ m s^{-1};

731   Table 3). The assumed values are approximately consistent with values of $<V_D>$ and v_w , in

732   Table 6, and with the V_D sign convention (Sect. 2.3). We also used $gs = 125$ m s^{-1} to scale

733   (virtually) the time axes in Fig. 9a and Fig. 10a to a horizontal distance. Within the scaled

734   coordinate frames, we assumed that all snow particle trajectories have negative slope ($\Delta z / \Delta x =$ -

735   1 m s^{-1} / 8 m s^{-1} = -0.12) and that all trajectories are stationary. However, both assumptions seem

736   inconsistent with the reflectivity structures in Fig. 5a, where positively-sloped particle fall

737   streaks are evident at $\sim$ 5500 m, inconsistent with Fig. 9a where positively-sloped fall streaks are

738   at $\sim$ 3500 m, and inconsistent with the positively-sloped fall streaks in Fig. 10a. On both flight

739   days, the fall streaks evince particle sources that move horizontally and with a horizontal speed

740   that is larger than the $v_w = 8$ m s^{-1} applied in the estimate of the trajectory slope. It may be that

741   the source's horizontal speed is comparable to the flight-level WKA-derived horizontal wind (27

742   to 32 m s^{-1}; Table 3) but we do not have data needed to verify that assertion. Based on the

743   assumption that snow particles followed the fall streaks while both were advecting horizontally,

744   we looked *downwind* of the hotplate - at a time later than t_0 in Fig. 9a and Fig. 10a - for particles

745   that became those that produced snowfall at the hotplate.

746   Particle images from 15 December 2016 were analyzed using the 2DP. With this

747   instrument the maximum all-in particle size (in the horizontal direction perpendicular to flight) is

748   6400 μm and the particle size resolution is 200 μm (Sect. 2.2). Within the time interval picked

749   for this analysis (discussed below), particles sizing in the smaller of the two spectral modes, with

750   mode size ~ 400 μm, were more numerous (results not shown). Because the 400 μm particles are

751   poorly resolved by the 2DP, and the same can be said for somewhat larger particles, those

752   smaller than 1000 μm were excluded from the following analysis. Figure 11a shows imagery

753   from 12 s of measurements acquired near the end of the sequence in Fig. 9a (00:01:02 to

754   00:01:14). This time interval was selected by tracing forward from t_0, along the slope of the fall

755   streaks, to the flight level. Many of the particles are rounded (indicating riming) and a few have

756   arms likely due to incomplete conversion of branched crystals to rimed snow particles. The mode

757   size corresponding to these images is 1600 μm. No liquid water was detected with these particles

758   (LWC $< 0.01 \times 10^{-3}$ kg m^{-3}; Fuller 2020; her Fig. 8), but liquid was detected, at ~ 00:00:00, as the

759   aircraft approached the ridgeline (Figs. 5a-b).

760   Turning to imagery from 3 January 2017, the most appropriate location for analysis

761   would be through the second billow structure evident in Fig. 10a (i.e., very close to the middle of

762   the Fig. 10a sequence). This billow sourced a fall streak that terminated at the hotplate (i.e., at

763   the time t_0 indicated in the figure). However, the aircraft only clipped the top of this billow, and

764   it was only when sampling the billow seen ~ 13 s earlier that larger ice particle concentrations (~

765   20,000 m^{-3}) (Fuller 2020; her Fig. 10) and larger LWC (~ 0.08×10^{-3} kg m^{-3}; Fig. 5d) were

766   detected. Maximum reflectivities were the same in all three billows (Z ~ 1 mm^6 m^{-3}; 0 dBZ), so it

767   was assumed that imagery collected in the first billow (20:32:00 to 20:32:02) was representative

768   of what was falling toward the hotplate. The 2DS was used to image these particles (Fig. 11b);

769   with this instrument the maximum all-in particle size (in the horizontal direction perpendicular to

770   flight) is 1280 μm and the size resolution is 10 μm (Sect. 2.2). Most of the objects in Fig. 11b

771   appear to be rimed and their mode size is ~ 400 μm. It is also noted that particles smaller than

772   100 μm were eliminated from these images, however, compared to the ~ 400 μm particles those

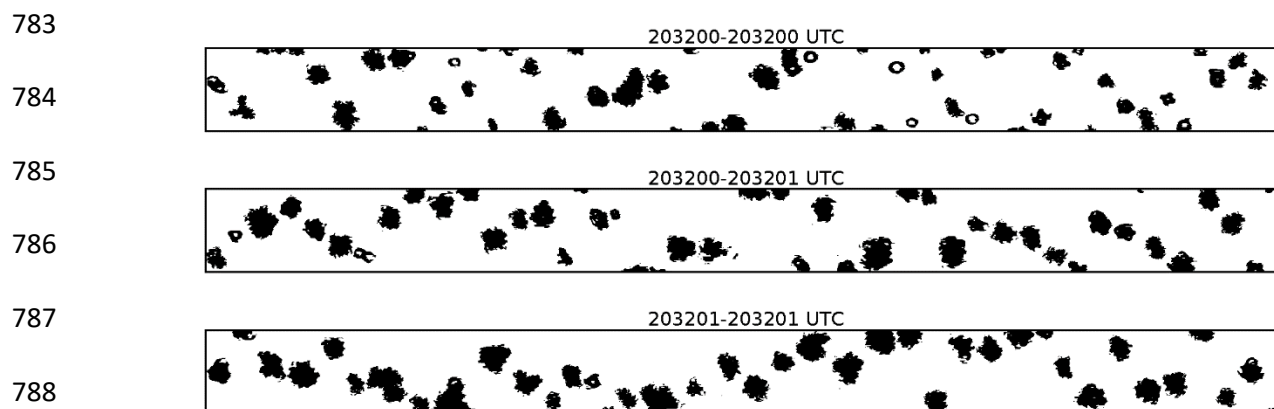773   smaller than 100 μm were significantly less abundant (results not shown).

774

775 (a)

240102-240106 UTC

240106-240111 UTC

240111-240114 UTC

781

782 (b)

783

203200-203200 UTC

203200-203201 UTC

203201-203201 UTC

789

790 Figure 11 – (a) 2DP particle imagery from 15 December 2016. The height of the strips is 6400

791 μm. These particles are estimated to be representative of those that fell from flight level toward

792 the hotplate. (b) 2DS particle imagery from 3 January 2017. The height of the strips is 1280 μm.

793 These particles are estimated to be representative of those that fell from flight level toward the

794 hotplate.

795

796 **3.7 – S/Z Relationships**

797   Our S/Z pairs are presented in Table 6 where the indexes ($i = 0$ and $i = 1$) are used to

798 indicate results derived for the averaging intervals. In the penultimate column of Table 6,

799 reflectivities are not corrected for attenuation, however, in the last column of Table 6 and in Fig.

800 12, the attenuation-corrected reflectivities are presented. Reflectivities from the penultimate

801 column of Table 6, attenuations from Table 4, and Eq. 1 were used to calculate the corrected

802 reflectivities. Also shown in Fig. 12 (black filled circles) is a subset of the S/Z pairs from PV11's

803 Fig. 11 ($0.01 < Z < 10$ mm^6 mm^{-3}) and the PV11 best-fit line (black). Results from PV11 are

804 specified as $S(\rho_1)/Z$ because those authors applied the lower of two density-size functions (ρ_1),

805 and the lower of two fall speed-size functions, with airborne measurements, in calculations of

806 snowfall rates (Sect. 1 and Table 1).

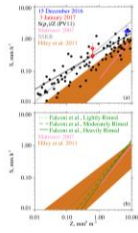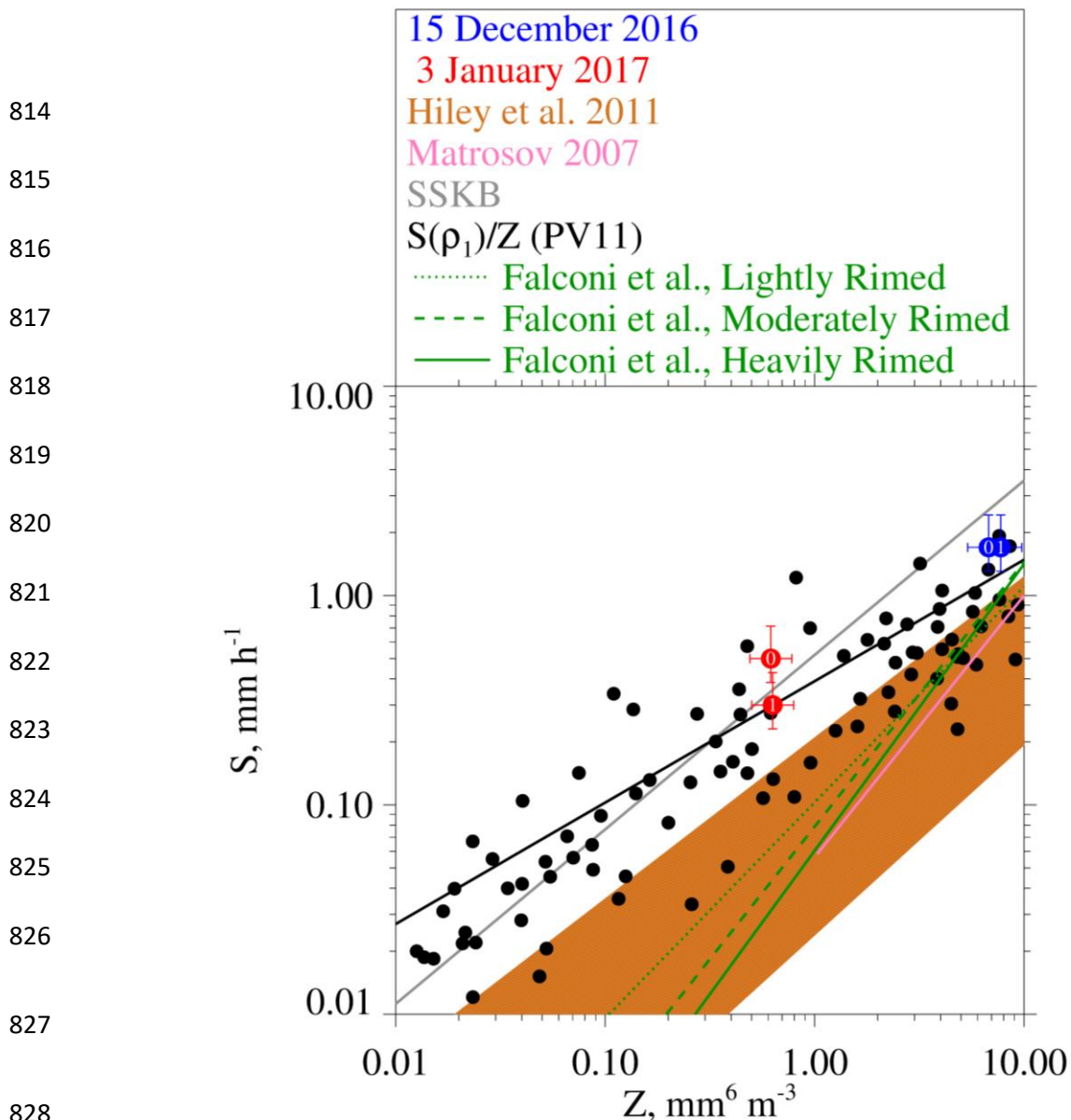807   THIS FIGURE WAS REVISED IN REVISION3.

808

809

810

811

812

813

Figure 12 – Snowfall rate versus radar reflectivity. Red and blue circles are plotted at attenuation-corrected reflectivities (Table 6) for the $i = 0$ and $i = 1$ averaging intervals. Error bars on these points represent precisions of the reflectivity (Sect. 2.3) and snowfall rate (Sect. 2.4) measurements. Also plotted are the S/Z relationship lines from Sect. 1 and Table 1. These are the S/Z lines defining the swath of S/Z relationships from Hiley et al. (2011), the S/Z relationship from Matrosov (2007), the S/Z relationship abbreviated SSKB, PV11's best-fit line, and the S/Z relationships from Falconi et al. (2018) (their Table 2). The $S(\rho_1)/Z$ points (black filled circles) are a subset from PV11's Fig. 11 ($0.01 < Z < 10$ mm^6 mm^{-3}).

837   There are two potential biases in the values of snowfall rate we tabulate (Table 6) and

838   plot (Fig. 12). First, the two snowfall events had flight-level vertical wind velocities (Figs. 5b

839   and 5d) that were positive (upward) upwind of the ridgeline, and vice versa downwind of the

840   ridgeline. Except for the strongest downdraft on 3 January 2017, the magnitude of this variance

841   is ~ 1 m s^{-1} (Figs. 5b and 5d). Assuming 1 m s^{-1} was the downward wind immediately over the

842   hotplate, the snow particles would have approached the HP gauge faster than their fall speed.

843   Our basis for stating this is fall speeds for the mode sizes discussed in Sect. 3.6 (1600 and 400

844   μm) and our assumption that the particles were graupel. (Table 7 has these characteristic sizes

845   and fall speeds.) However, the conjectured downdraft speed is likely an overestimate - because

846   of divergence occurring as the draft approached the surface - and because the sizes in Table 7

847   likely underestimate what fell to the hotplate. Relevant to the last of these assertions, we used the

848   altitude/T/RH measurements (Table 3) to calculate the vertical distance available for growth via

849   riming, and thus for a fall speed increase, between the flight level and the lifted condensation

850   level. Assuming an adiabatically-stratified liquid cloud and unit collection efficiency (these

851   assumptions overestimate growth by riming), and no change of particle crossection

852   (underestimates growth by riming), our calculations indicate that relative increases of size and

853   fall speed were 40 and 20 %, respectively, on 3 January 2017, and that these relative increases

854   were a factor-of-two larger on 15 December 2016.

855

856   Table 7 – Estimates of snow particle fall speed

Date	Mode Size, μm	Assumed Particle Type	Fall Speed, m s^{-1}	Reference
15 December 2016	1600	graupel	1.4	PV11; assuming ρ_1 in their Fig. 5
3 January 2017	400	graupel	0.7	PV11; assuming ρ_1 in their Fig. 5

857
858

859   Second, there is concern that values of S from 3 January 2017 are underestimated.

860   Although values of S must be > 0, we presented 1 Hz values (gray points, Fig. 8) approaching -

861   0.3 mm h^{-1}. Negative values resulted because we did not impose a threshold of 0 mm h^{-1} on the

862   uncorrected snowfall rates (this thresholding is discussed in Z18) and because negative snowfall

863   rate values (uncorrected for catch inefficiency) are amplified by the gauge-catch correction (Sect.

864   2.4). The implication is that 0.2 mm h^{-1} could be added to the one-minute averaged values of

865   snowfall rate in Table 6 and in Fig. 12. Here, the assumption is that an averaged S of -0.2 mm h^{-}

866   ^{1}, in Fig. 8, indicates no snowfall at the hotplate; however, because the hotplate was operated

867   autonomously (Sect. 2.1) we have no way to verify the assumption.

868

869   **4 – Results**

870   Figure 12 shows our four snowfall rate/reflectivity pairs (red and blue circles) after the

871   reflectivities were corrected for attenuation. The error bars on these data pairs represent the

872   precision of the Z measurement (Sect. 2.3) and the precision of the S measurement (Sect. 2.4).

873   Presentation clarity was what guided the selection of S and Z axis ranges in this figure but with

874   the consequence that 32 of PV11's S/Z pairs are not shown because they plot at $Z > 10 \text{ mm}^6 \text{ m}^{-3}$.

875   The way that the PV11 data pairs scatter closest to $Z = 10 \text{ mm}^6 \text{ m}^{-3}$, combined with the fact that

876   the PV11 data pairs at $Z > 10 \text{ mm}^6 \text{ m}^{-3}$ are not shown, could lead to the interpretation that the

877   slope describing the best-fit relationship, at Z approximately $> 2 \text{ mm}^6 \text{ m}^{-3}$, should be decreased

878   relative to the actual slope of the PV11 best-fit line. Readers who view PV11's Fig. 11 will

879   conclude that this interpretation is not warranted.

880   As is discussed in Sect. 1, computation-based W-band S/Z relationship have inputs from

881   parameterized descriptions of density, shape, fall speed, PSD, and particle size. The

882   computation-based S/Z relationships are in the top three rows of Table 1; the subsequent two

883   rows of Table 1 have S/Z relationships that resulted from a hybridization of measurements and

884   calculations (PV11 and Falconi et al. 2018).

885   We now compare our snowfall rates (fourth column of Table 6) to snowfall rates where

886   they plot on an S/Z relationship line evaluated at one of our attenuation-corrected reflectivities.

887   The departure between these is reported as a relative S difference expressed as $|(S_{HP}-S)|/S$ where

888   S_{HP} is from Table 6 and where S is on an S/Z relationship line. All possible comparisons are

889   presented graphically in Fig. 12. Table 1 has both the minimum relative S differences and the

890   salient maximum relative S differences. The comparisons will be discussed in the order of

891   presentation in Table 1.

892   In comparisons of our snowfall rates and the upper-limit S/Z relationship line from Hiley

893   et al. (2011) the relative difference is no smaller than 0.7 and 1.0 on 15 December and 3 January,

894   respectively. These minimum relative differences exceed the hotplate precision (Sect. 2.4) by at

895   least a factor of two. It is concluded that our paired values of undercatch-corrected precipitation

896   rate and attenuation-corrected radar reflectivity provide evidence that a calculation of S based on

897   the Hiley et al. (2011) upper-limit, when applied to rimed snow particles, is associated with a

898   low-biased estimate of S. A retrieval based on Hiley et al.'s average S/Z relationship (not

899   shown), which bisects the orange region in Fig. 12, corresponds to an even larger low bias. This

900   is a concern because Hiley et al. (2011) used their average S/Z relationship to retrieve global

901   snowfall distributions and since global observations reported in Wang et al. (2013) document the

902   frequent occurrence of supercooled liquid within snowing clouds.

903   Figure 12 shows the separation between our measurements and the Matrosov (2007)

904   calculation. The separation is about a factor of two (minimum relative difference = 1.4) for the

905   points obtained on 15 December 2016 and corresponds to an underestimation of S (low bias)

906   when compared to our measurements. The points from 3 January 2017 plot at an attenuation-

907   corrected reflectivity smaller than the lower-limit of the calculation (Matrosov 2007). Since the

908   particle images (Fig. 11a-b) reveal no evidence of the particle type modeled by Matrosov (2007)

909   (aggregates), it is not surprising that the Matrosov S/Z relationship is not representative of our

910   measurements.

911   One plausible reason for the low bias discussed in the previous two paragraphs is the

912   smaller density implicit in most computationally-based S/Z relationships and especially those

913   which assume that snow particles are crystals. Densities are quite different for crystals versus

914   that for rimed snow particles. For example, in Brown and Francis (1995), assuming a 2 mm

915   crystal, the density is ~ 30 kg m^{-3}, whereas in PV11 (their Eq. 1), assuming a 2 mm graupel

916   particle, the density is ~ 200 kg m^{-3}. Because aggregates are collections of crystals, this

917   comparison of crystal and graupel densities also seems relevant to a comparison of graupel and

918   aggregate snow particle densities.

919   Figure 12 compares our S_{HP}/Z' data pairs to the SSKB S/Z relationship line and Table 1

920   presents the relative differences between the data pairs and the SSKB line. Compared to the S/Z

921   relationship represented by the top of the orange region in Fig. 12, and compared to the Matrosov

922   2007 relationship, the SSKB line plots closer to our data points (minimum relative difference ~

923   0.3). We note that the only instances of $S_{HP} < S$ are three of four comparisons of our

924   measurements to the SSKB relationship. A possible reason for this is that the density applied in

925   SSKB (Table 1) is not entirely representative of conditions during our study. An analysis of the

926   sensitivity of the SSKB to a change in density is needed to investigate our assertion.

927   Comparisons of our S_{HP}/Z' data pairs and PV11's best-fit line are also in Table 1. The

928   table demonstrates that the agreement is reasonable - minimum relative difference no larger than

929   0.3 – and Fig. 12 shows that our data pairs plot at or above the PV11 best fit line.

930   Based on data from PV11 and our S_{HP}/Z' data pairs, as well as the S/Z relationship

931   abbreviated SSKB, it is expected that the S/Z relationships reported by Falconi et al. (2018) for

932   rimed snow particles (Sect. 1) would plot higher in S-versus-Z space than is illustrated in Fig. 12.

933   Notably, only the upper-end of the Falconi et al. lines (i.e., at $Z > 8$ mm^6 m^{-3}) plot above the

934   upper-limit that Hiley et al. (2011) developed for unrimed snow particles. A plausible

935   explanation for the lower-than-expected S/Z relationships of Falconi et al. is now offered.

936   Falconi et al. used liquid water path as a proxy for the extent of snow particle riming (von Lerber

937   et al. 2017). A consequence may have been that the proxy did not dependably exclude unrimed

938   snow particles (crystals and aggregates) from the riming categories of Falconi et al. If this was

939   the case, then the data groupings that were the basis for the Falconi et al. S/Z relationships may

940   have been affected. When applying the heavily-rimed S/Z relationship of Falconi et al. with our

941   S_{HP} / Z' data pairs we find that the minimum relative differences are 0.6 (December 15) and 8.5

942   (January 3) (Table 1). Additionally, the differences are 0.5 (December 15) and 5.9 (January 3)

943   when applying the moderately-rimed S/Z relationship of Falconi et al. (results not shown).

944   Further research is needed to resolve the reason for the mismatch between the snowfall

945   rate/reflectivity pairs reported here and the S/Z relationships reported in Falconi et al.

946   Our conclusion that the upper-limit S/Z relationship from Hiley et al. (2011)

947   underestimates S would be modified if our WCR-derived reflectivities were negatively biased.

948   Assuming the reflectivities are negatively biased by 2.5 dBZ, the minimum relative differences

949   discussed previously are no smaller than 0.1 and 0.3 on 15 December and 3 January,

950   respectively. A bias in reflectivity of this magnitude cannot be ruled out but neither can a

951   positive bias of the same magnitude (Sect. 2.3). The latter increases the minimum relative

952   differences to 1.6 and 2.2 on 15 December and 3 January, respectively. In each of these

953   calculations we have summed the attenuations (Table 4) with ± 2.5 dBZ and used Eq. 1 to

954   calculate error-perturbed reflectivities.

955   The scatter of measurements in Fig. 12, the plausibility of a -2.5 to +2.5 dBZ bias in

956   WCR reflectivity measurements, and error in measurement of S (Sect. 2.4), indicate that refined

957   techniques will be needed in future investigations which apply the approach described here.

958   Taking into consideration the goal of evaluating snowfall rates from space, some advance in

959   satellite remote sensing also seems warranted. One issue is diagnosing where riming is occurring

960   within clouds. Both lidars and radiometers can sense supercooled liquid water from space (e.g.,

961   Battaglia and Panegrossi, 2020), and if combined with Doppler radars operating at multiple

962   wavelengths, can diagnose precipitation attributable to rimed snow particles. Despite limitations

963   of the multiple-wavelength Doppler method, for example in scenarios with vertical air speed

964   comparable to and larger than particle fall speed (Vogl et al. 2022), the method has been

965   validated in ground-based field studies (Kneifel et al. 2015; Mason et al. 2018). Technical

966   challenges also remain for implementing the method from space (Battaglia et al. 2020).

967   **5 – Conclusions**

968   We have reported surface measurements of S and near-surface measurements of Z. The

969   latter came from overflights of a ground site, where a precipitation gauge was operated, and were

970   acquired using an airborne W-band radar. The values of Z were corrected for attenuation.

971   The reported S_{HP}/Z' pairs plot at or above the S-versus-Z best-fit line of PV11 (Fig. 12)

972   and the minimum relative S difference (Table 1) is no larger than 0.3. The PV11 data came from

973   airborne measurements of W-band reflectivity, acquired within $\pm$ 100 m of flight level, and from

974   coincident measurements of snow particle imagery. PV11 used a density-size function and a fall

975   speed-size function, and measurements (PSD and particle images) to calculate S for snow

976   particles that were classified as both rimed crystals and graupel. This classification is also

977   consistent with the particle imagery we have presented (Fig. 11).

978   We have documented a substantial difference in comparisons between our snowfall rates

979   and reflectivity-dependent S values calculated using an upper-limit S/Z relationship for unrimed

980   snow particles (Hiley et al. 2011). Here the minimum relative S differences are 0.7 and 1.0 for

981   our two overflights and in a comparison to our measurements correspond to an underestimation

982   of snowfall rate (Fig. 12). The relative differences are approximately a factor of two larger than

983   the precision of our snowfall rate measurement. We also report a substantial difference, and S

984   underestimation compared to our measurements (Fig. 12), for the comparison made to an S/Z

985   relationship which assumes the snow particles are aggregates (Matrosov 2007). The snowfall rate

986   underestimates obtained using both Hiley et al.'s and Matrosov's S/Z relationships (Fig. 12) are

987   perhaps expected given that the density factored into those S/Z calculations is small compared to

988   that for rimed snow particles. It is also expected that the larger density and spherical shape

989   applied in the SSKB S/Z relationship contributed to the better agreement (minimum relative

990   difference ~ 0.3) with our S_{HP}/Z' pairs. Our conclusion is that some snowfall retrievals (e.g.,

991   Hiley et al. 2011) will underestimate S for weather targets containing rimed snow particles. We

992   also state that our conclusion is at odds with measurements and analysis in Falconi et al. Those

993   researchers reported S/Z relationships for rimed snow particles which in instances with Z < 8

994    $mm^6 m^{-3}$ plot below the upper-limit of Hiley et al. (Fig. 12). The consequence is that the

995   minimum relative S difference in our comparison to Falconi et al. (assuming Falconi et al.'s

996   heavily-rimed classification) is comparable to and larger than in our comparison to the Hiley et

997   al.'s upper-limit S/Z relationship.

998   New research is needed to refine the S/Z relationship for rimed snow particles. This could

999   be computational – e.g., investigation of the utility of parameterizing S in terms of both Z and

1000   density – or could be observational. Unlike the investigation of PV11, where only an airborne

1001   platform was employed, we have demonstrated that useful information can be obtained using

1002   coordinated ground-based and airborne systems. Another approach would be with only ground-

1003   based instrumentation. This would avoid some of the complications encountered in this study,

1004   including W-band attenuation and a reliance on particle imagery acquired aloft. A study with

1005   both ground-based and airborne systems would also be useful for understanding an S/Z

1006   mismatch apparent at $Z < 8$ mm^6 m^{-3}. Elements of the mismatch are the measurements reported

1007   here, PV11's best-fit line, and the measurement-based S/Z relationships reported by Falconi et al.

1008   (2018). These three research teams reported measurements relevant to the development of an S/Z

1009   relationship for rimed snow particles.

1010   **6 – Appendix**

1011   This appendix explains how HP (hotplate) and WCR (Wyoming Cloud Radar) averages

1012   were evaluated. The scheme starts with an HP averaging interval (duration 60 s) and derives a

1013   WCR averaging interval and a WCR averaging domain. The latter encompasses a subset of the

1014   altitude-time crossection sampled by the WCR. The top boundary of the domain was derived

1015   using vertical-component Doppler velocities within the interval/domain. Because of this

1016   dependence, the line defining the top boundary was derived iteratively.

1017   With the overflight time symbolized t_0, the beginning and ending times of two 60-second

1018   HP averaging intervals are

1019 $$t_{HP,B} = t_O \qquad \qquad \text{(A1)}$$

1020 $$t_{HP,E} = t_O + 60 \qquad \qquad \text{(A2)}$$

1021   Since two adjacent HP averaging intervals are evaluated in this analysis, we express the

1022   averaging times with the following recursive equations

1023 $$t_{HP,B}(i) = t_O + i \cdot 60 \qquad \qquad \text{(A3)}$$

1024   and

1025 $$t_{HP,E}(i) = t_O + (i+1) \cdot 60 . \qquad \qquad \text{(A4)}$$

1026   In Eqs. A3-A4 the index is $i \in \{0, 1\}$. A special case with $i = 2$ is also analyzed (Sect. 3.5).

1027   Analogous to the recursion in Eq. A4, the ending time of a WCR averaging interval is

1028 $$t_{WCR,E}(i) = t_O - i \cdot 60 \cdot v_w / gs .$$ (A5)

1029   Here v_w is a wind advection speed (discussed below) and the second term on the rhs is a wind

1030   advection distance divided by the WKA (Wyoming King Air) ground speed (gs). Analogous to

1031   the Eq. A5, the beginning time of a WCR averaging interval is

1032 $$t_{WCR,B}(i) = t_{WCR,E} - (i+1) \cdot 60 \cdot v_w / gs$$ (A6)

1033   The wind advection speed (v_w) in Eqs. A5-A6 was calculated using an altitude-

1034   dependent west-to-east wind velocity (u) and an altitude-dependent south-to-north wind velocity

1035   (v). These altitude-dependent component velocities were calculated using the horizontal wind

1036   vectors in the penultimate and last columns of Table 3. Plots of the component velocities versus

1037   altitude and the linear functions used to relate component velocities to altitude are presented in

1038   Figs. A1a-b.

1039   An altitude ($z' = 3400$ m) was assumed for evaluating the horizontal wind advection

1040   vector. This is the altitude of the ridges west and northwest of the HP site (Figs. 3a-b).

1041   The WKA track vector (Table 3) defines the vertical plane of the WCR measurements.

1042   We assumed that wind advection of snow particles occurred parallel to this vector. With the

1043   assumption stated in the previous paragraph, the horizontal wind advection speed (v_w) was

1044   calculated as the projection of the horizontal wind vector onto the track vector.

1045 $$v_w = \frac{u(z') \cdot gs_x + v(z') \cdot gs_y}{\left(gs_x^2 + gs_y^2 \right)^{1/2}}$$ (A7)

1046   In Eq. A7 the west-to-east and south-to-north components of the track vector are symbolized gs_x

1047   and gs_y. Vector representations of the track vector are in Table 3. On 14/15 December 2016 and

1048   3 January 2017, the values of v_w are 7.4 and 8.9 m s^{-1}, respectively.

1049   In addition to the properties gs and v_w used to evaluate Eqs. A5-A6, a WCR averaging

1050   interval/domain was evaluated using a snow particle downward speed (Eq. A8).

1051 $v_p = |<V_D>| + \sigma_{V_D}$ (A8)

1052   Here, $<V_D>$ is the average of Doppler velocities within an averaging interval/domain,

1053 $|<V_D>|$ is the absolute value of the average, and σ_{V_D} is the standard deviation of the average.

1054   On both the lhs and rhs of Eq. A8, all terms are greater than zero.

1055   We interpret v_p as the maximum likely snow particle speed toward the ground. There are

1056   three reasons for this: 1) For the WCR averaging intervals/domains we analyzed, values of

1057 $<V_D>$ were consistently less than zero (Table 6). This indicates that snow particles (on

1058   average) were moving toward the ground. 2) Again, for the WCR averaging intervals/domains

1059   we analyzed, σ_{V_D} was comparable to $|<V_D>|$. This indicates that turbulent eddies transported

1060   snow particles upward and downward at a speed comparable to their downward speed in still air.

1061   3) The V_D are reflectivity weighted (Haimov and Rodi 2013) and are thus indicative of the

1062   motion of the largest particles within an averaging interval/domain.

1063   We now focus on the top boundary of a WCR averaging interval/domain. Figures 6b and

1064   6d have representations of the boundary. The slope defining this boundary was calculated as

1065 $-v_p \cdot gs / v_w$. That is, particles below this boundary moved downward sufficiently fast and

1066   horizontally sufficiently slow to advect reasonably close to the hotplate. Starting with diagnosed

1067   values of gs and v_w, the values of v_p and slope, were derived iteratively. The precision of the

1068   derived v_p is $\pm\,0.1$ m s^{-1}.
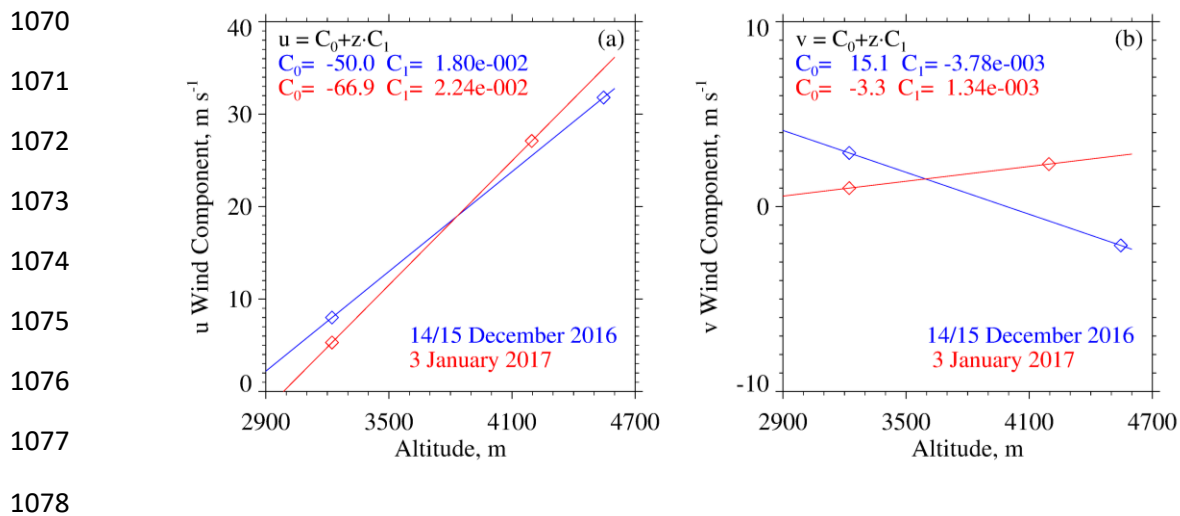
1069

Figure A1 – (a) West-to-east (u) wind velocity derived using measurements from the WKA and the AmeriFlux (AF) tower. Also shown is the linear function used to relate u to altitude. (b) South-to-north (v) wind velocity derived using measurements from the WKA and AF. Also shown is the linear function used to relate v to altitude. WKA and AF velocities are presented as vectors in the penultimate and last columns of Table 3.

1085   Data Availability. The WKA and WCR measurements can be obtained from the SNOWIE data

1086   archive of NCAR/EOL, which is sponsored by the National Science Foundation. Hotplate gauge

1087   measurements are at https://doi.org/10.15786/20103146. The US-GLE AmeriFlux measurements

1088   are at https://ameriflux.lbl.gov/. The Brooklyn Lake SNOTEL gauge measurements are at

1089   https://www.wcc.nrcs.usda.gov/snow/. Merged Hotplate, SNOTEL, and AmeriFlux data

1090   sequences from 14/15 December 2016 and 3 January 2017 are in Snider (2023).

1091

1096

References

AmeriFlux, https://ameriflux.lbl.gov/, 2021

Battaglia, A. and Panegrossi, G., What Can We Learn from the CloudSat Radiometric Mode Observations of Snowfall over the Ice-Free Ocean?, 12, 3285, https://doi.org/10.3390/rs12203285, 2020

Battaglia, A., Tanelli, S., Tridon, F., Kneifel, S., Leinonen, J., and Kollias, P, Triple-Frequency Radar Retrievals, In: Levizzani, V., Kidd, C., Kirschbaum, D.B., Kummerow, C.D., Nakamura, K., Turk, F.J. (eds) *Satellite Precipitation Measurement*, Advances in Global Change Research, vol 67. Springer, Cham. https://doi.org/10.1007/978-3-030-24568-9_13, 2020

Boudala, F.S., R. Rasmussen, G.A. Isaac, and B. Scott, Performance of Hot Plate for Measuring Solid Precipitation in Complex Terrain during the 2010 Vancouver Winter Olympics, J. Atmos. Oceanic Technol., 31, 437–446, https://doi.org/10.1175/JTECH-D-12-00247.1, 2014

Braham , R. R., Snow Particle Size Spectra in Lake Effect Snows. J. Appl. Meteor. Climatol., 29, 200–207, https://doi.org/10.1175/1520-0450(1990)029<0200:SPSSIL>2.0.CO;2, 1990

Brock, F. V., and Richardson, S. J., Meteorological Measurement Systems, Oxford University Press, New York, 304 pp., 2001

Brown, P. R. A., and P. N. Francis, Improved Measurements of the Ice Water Content in Cirrus Using a Total-Water Probe. J. Atmos. Oceanic Technol., 12, 410–414, https://doi.org/10.1175/1520-0426(1995)012<0410:IMOTIW>2.0.CO;2., 1995

Cocks, S.B., S.M. Martinaitis, B. Kaney, J. Zhang, and K. Howard, MRMS QPE Performance during the 2013/14 Cool Season, J. Hydrometeor., 17, 791–810, https://doi.org/10.1175/JHM-D-15-0095.1, 2016

Faber, S., French, J. R., and Jackson, R., Laboratory and in-flight evaluation of measurement uncertainties from a commercial Cloud Droplet Probe (CDP), Atmos. Meas. Tech., 11, 3645–3659, https://doi.org/10.5194/amt-11-3645-2018, 2018

Falconi, M. T., von Lerber, A., Ori, D., Marzano, F. S., and Moisseev, D.: Snowfall retrieval at X, Ka and W bands: consistency of backscattering and microphysical properties using BAECC ground-based measurements, Atmos. Meas. Tech., 11, 3059–3079, https://doi.org/10.5194/amt-11-3059-2018, 2018

1133   Field, P.R., Hogan, R.J., Brown, P.R.A., Illingworth, A.J., Choularton, T.W. and Cotton, R.J.,
1134   Parametrization of ice-particle size distributions for mid-latitude stratiform cloud. Q.J.R. Meteorol.
1135   Soc., 131: 1997-2017. https://doi.org/10.1256/qj.04.134, 2005

1136   Fuller, S.E., Improvement of the Snowfall / Reflectivity Relationship for W-band Radars, MS Thesis,
1137   Department of Atmospheric Science, University of Wyoming, 2020

1138   Geerts, B., Q. Miao, Y. Yang, R. Rasmussen, and D. Breed, An Airborne Profiling Radar Study of the
1139   Impact of Glaciogenic Cloud Seeding on Snowfall from Winter Orographic Clouds, J. Atmos. Sci.,
1140   67, 3286–3302, https://doi.org/10.1175/2010JAS3496.1, 2010

1141   Haimov, S., and Rodi, A., Fixed-Antenna Pointing-Angle Calibration of Airborne Doppler Cloud Radar,
1142   Journal of Atmospheric and Oceanic Technology, 30, 2320-2335, https://doi.org/10.1175/JTECH-
1143   D-12-00262.1, 2013

1144   Hiley, M. J., M. S. Kulie, and R. Bennartz, Uncertainty Analysis for CloudSat Snowfall Retrievals, J. Appl.
1145   Meteor. Climatol., 50, 399–418, 2011

1146   Kneifel, S., von Lerber, A., Tiira, J., Moisseev, D., Kollias, P., and Leinonen, J., Observed relations between
1147   snowfall microphysics and triple-frequency radar measurements. J. Geophys. Res. Atmos., 120,
1148   6034– 6055, doi: 10.1002/2015JD023156, 2015

1149   Kochendorfer, J., Nitu, R., Wolff, M., Mekis, E., Rasmussen, R., Baker, B., and Jachcik, A, Testing and
1150   development of transfer functions for weighing precipitation gauges in WMO-SPICE, Hydrology
1151   and Earth System Sciences, 2, 1437-1452, https://doi.org/10.5194/hess-22-1437-2018, 2018

1152   Korolev, A. V., E. F. Emery, J. W. Strapp, S. G. Cober, G. A. Isaac, M. Wasey, and D. Marcotte, Small ice
1153   particles in tropospheric clouds: Fact or artifact? Airborne Icing Instrumentation Evaluation
1154   Experiment, Bull. Amer. Meteor. Soc., 92, 967–973, https://doi.org/10.1175/2010BAMS3141.1,
1155   2011

1156   Kulie, M. S., and R. Bennartz, Utilizing Spaceborne Radars to Retrieve Dry Snowfall, J. Appl. Meteor.
1157   Climatol., 48, 2564–2580, https://doi.org/10.1175/2009JAMC2193.1, 2009

1158   Kulie, M. S., Milani, L., Wood, N. B., Tushaus, S. A., Bennartz, R., and L'Ecuyer, T. S., A Shallow
1159   Cumuliform Snowfall Census Using Spaceborne Radar, Journal of Hydrometeorology, 4, 1261-
1160   1279, https://doi.org/10.1175/JHM-D-15-0123.1, 2016

1161   Lawson, R. P., O'Connor, D., Zmarzly, P., Weaver, K., Baker, B., Mo, Q., and Jonsson, H., The 2D-S
1162   (Stereo) Probe: Design and Preliminary Tests of a New Airborne, High-Speed, High-Resolution

Particle Imaging Probe, J. Atmos. Ocean. Tech., 23, 1462–1477, https://doi.org/10.1175/JTECH1927.1, 2006

Liebe, H.J., Manabe, T., and Hufford, G.A., Millimeter–wave attenuation and delay rates due fog/cloud conditions, IEEE Trans. Antenn. Propag., 37, 1617–1623, 1989

Liu, C.-L., and A. J. Illingworth, Toward more accurate retrievals of ice water content from radar measurements of clouds, J. Appl. Meteor., 39, 1130–1146, 2000

Locatelli, J.D. and Hobbs, P.V., Fall speed and masses of solid precipitation particles, J. Geophys. Res., 79, 2185–2197, https://doi.org/10.1029/JC079i015p02185, 1974

Macklin, W.C., The density and structure of ice formed by accretion, Q.J.R.Meteorol.Soc., 88: 30-50. doi:10.1002/qj.49708837504, https://doi.org/10.1002/qj.49708837504, 1962

Marlow, S.A, J.M. Frank, M. Burkhart, B. Borkhuu, S.E. Fuller, and J.R. Snider, Snowfall Measurements at Wind-exposed and Sheltered Sites in the Rocky Mountains of Southeastern Wyoming, in revision for the Journal of Applied Meteorology and Climatology, http://www-das.uwyo.edu/~jsnider/manuscript_revision2.docx, 2023

Martinaitis, S.M., S.B. Cocks, Y. Qi, B.T. Kaney, J. Zhang, and K. Howard, Understanding winter precipitation impacts on automated gauge observations within a real-rime system, J. Hydrometeor., 16, 2345-2363, https://doi.org/10.1175/JHM-D-15-0020.1, 2015

Mason, S. L., Chiu, C. J., Hogan, R. J., Moisseev, D., and Kneifel, S., Retrievals of riming and snow density from vertically pointing Doppler radars, Journal of Geophysical Research: Atmospheres, 123, 13,807– 13,834, https://doi.org/10.1029/2018JD028603, 2018

Matrosov, S.Y., Modeling Backscatter Properties of Snowfall at Millimeter Wavelengths, J. Atmos. Sci., 64, 1727-1736, https://doi.org/10.1175/JAS3904.1, 2007

Nemarich, J., Wellman, R.J., and Lacombe, J., Backscatter and attenuation by falling snow and rain at 96, 140, and 225 GHz, IEEE Trans. Geosci. Remote, 26, 319–329, 1988

Panofsky, H.A. and Dutton, J.A., *Atmospheric Turbulence*, Wiley-Interscience, New York, 397 pp., 1984

Pokharel, B. and G. Vali, Evaluation of Collocated Measurements of Radar Reflectivity and Particle Sizes in Ice Clouds, J. Appl. Meteor. Climatol., 50, 2104–2119, https://doi.org/10.1175/JAMC-D-1005010.1, 2011

1191 Rasmussen, R.M., J. Hallett, R. Purcell, S.D. Landolt, and J. Cole, The Hotplate precipitation gauge, J.
1192   Atmos. Oceanic Technol., 28, 148-164, https://doi.org/10.1175/2010JTECHA1375.1, 2011

1193 R.M. Young Company, Model 05103 Wind Monitor, 2001

1194 Skofronick-Jackson, G., and Coauthors, The Global Precipitation Measurement (GPM)   Mission   for
1195   science and society, Bull. Amer. Meteor. Soc., 98, 1679–1695, https://doi.org/10.1175/BAMS-D-
1196   15-00306.1, 2017

1197 Smith, P.L., Equivalent radar reflectivity factors for snow and ice particles, J. Climatol. Appl. Meteor., 23,
1198   1258–1260, https://doi.org/10.1175/1520-0450(1984)023<1258:ERRFFS>2.0.CO;2, 1984

1199 Snider, J.R., Supplemental dataset for Marlow et al. (2023), https://doi.org/10.15786/20247870, 2023

1200 Surussavadee, C., and D. H. Staelin, Millimeter-Wave Precipitation Retrievals and Observed-versus-
1201   Simulated Radiance Distributions: Sensitivity to Assumptions. J. Atmos. Sci., 64, 3808–3826,
1202   https://doi.org/10.1175/2006JAS2045.1, 2007

1203 Tessendorf, S. A., and Coauthors, A transformational approach to winter orographic weather modification
1204   research: The SNOWIE Project, Bulletin of the American Meteorological Society, 100, 71–92,
1205   https://doi.org/10.1175/BAMS-D-17-0152.1, 2019

1206 Ulaby, F.T., Moore, R.K., and Fung, K., Microwave Remote Sensing: Active and Passive, Vol. 1,
1207   Microwave Remote Sensing Fundamentals and Radiometry, ARTECH HOUSE Inc., Norwood,
1208   MA, p. 456., 1981

1209 Vali, G. and Haimov, S., Observed extinction by clouds at 95 GHz, IEEE Trans. Geosci. Remote, 39, 190–
1210   193, 2001

1211 Vogl, T., Maahn, M., Kneifel, S., Schimmel, W., Moisseev, D., and Kalesse-Los, H.: Using artificial neural
1212   networks to predict riming from Doppler cloud radar observations, Atmos. Meas. Tech., 15, 365–
1213   381, https://doi.org/10.5194/amt-15-365-2022, 2022

1214 von Lerber, A., D. Moisseev, L. F. Bliven, W. Petersen, A. Harri, and V. Chandrasekar: Microphysical
1215   Properties of Snow and Their Link to Ze–S Relations during BAECC 2014. J. Appl. Meteor.
1216   Climatol., 56, 1561–1582, https://doi.org/10.1175/JAMC-D-16-0379.1, 2017

1217 Wang,Y., G.Liu, E.Seo, and Y.Fu, Liquid water in snowing clouds: Implications for satellite remote

1218 sensing of snowfall, Atmos. Res., 60-72, 10.1016/j.atmosres.2012.06.008, 2013

1219 Wang, P.K., and W. Ji, Collision Efficiencies of Ice Crystals at Low–Intermediate Reynolds Numbers
1220   Colliding with Supercooled Cloud Droplets: A Numerical Study, Journal of the Atmospheric
1221   Sciences, 57, 1001-1009, https://doi.org/10.1175/1520-0469(2000)057<1001:CEOICA>2.0.CO;2,
1222   2000

1223 Wilson, J., and E. Brandes, Radar measurement of rainfall—A summary, Bull. Amer. Meteor. Soc., 60,
1224   1048–1058, https://doi.org/10.1175/1520-0477(1979)060<1048:RMORS>2.0.CO;2, 1979

1225 Wolfe, J.P., and J.R. Snider, A relationship between reflectivity and snow rate for a high-altitude S-band
1226   radar, J. Appl. Meteor. Climatol., 51, 1111–1128, https://doi.org/10.1175/JAMC-D-11-0112.1,
1227   2012

1228 Zaremba, T.J., and Coauthors, Vertical motions in orographic cloud systems over the Payette River Basin.
1229   Part 1: Recovery of vertical motions and their uncertainty from airborne Doppler radial Velocity
1230   Measurements, in press at the Journal of Applied Meteorology and Climatology,
1231   https://doi.org/10.1175/JAMC-D-21-0228.1, 2022

1232 Zelasko, N., Wettlaufer, A., Borkhuu, B., Burkhart, M., Campbell, L. S., Steenburgh, W. J., and Snider,
1233   J.R., Hotplate precipitation gauge calibrations and field measurements, Atmos. Meas. Tech., 11,
1234   441-458, https://doi.org/10.5194/amt-11-441-2018, 2018

1235 Zikmunda, J. and Vali, G., Fall patterns and fall velocities of rimed ice crystals, J. Atmos. Sci., 29, 1334–
1236   1347, https://doi.org/10.1175/1520-0469(1972)029<1334:FPAFVO>2.0.CO;2, 1972

1237